2013

Carbon Sequestration Potential of the Coast Range Ophiolite in California

Daniel C. Carnevale
University of Rhode Island, dcarnevale@gmail.com

CARBON SEQUESTRATION POTENTIAL OF THE COAST RANGE OPHIOLITE IN CALIFORNIA

BY

DANIEL C. CARNEVALE

A THESIS SUBMITTED IN PARTIAL FULFILLMENT OF THE

REQUIREMENTS FOR THE DEGREE OF

MASTER OF SCIENCE

IN

ENVIRONMENTAL AND EARTH SCIENCES

UNIVERSITY OF RHODE ISLAND

2013

MASTERS OF SCIENCE THESIS

OF

DANIEL C. CARNEVALE

APPROVED:

Thesis Committee:

Major Professor: Dr. Dawn Cardace_____

Dr. Brian Savage_____

Dr. Arthur Spivack _____

Dr. Mark H. Stolt _____

Dean of the Graduate School: Dr. Nasser H. Zawia_____

UNIVERSITY OF RHODE ISLAND

2013

Abstract

A number of methods of drawing down atmospheric carbon dioxide are being investigated as a result of concerns over the impacts of global warming. Mineral carbonation is a proven manner of sequestering carbon dioxide and functions by binding carbon dioxide with iron-, calcium-, and magnesium-containing minerals—including olivine, pyroxene, and serpentine— to form carbonate minerals. The Coast Range Ophiolite (CRO) in California is a 700 km long body of ultramafic rocks containing vast amounts of olivine and serpentine. By assessing the mineralogical and geochemical characteristics of the minerals in these rocks, I assess the potential quantity of CO_2 that could be sequestered in these rocks.

Olivine is the most ideal mineral reactant for carbon sequestration, based on abundance and reactivity. My data show that the first 45 m of surface rocks of the CRO contain very little olivine, but petrography shows olivine at least 110 m below the surface, and olivine has been previously identified in various sections of the CRO. Using energy-dispersive x-ray spectroscopy, I showed that the amount of Mg in olivine in the rocks is 24% and the amount of total Mg + Fe + Ca is 38%. Based on these figures and volume, density, and the percentage of rock reacted with CO_2, I calculate that the CRO can sequester ~ 6.9×10^{13} kg CO_2 for Mg-only sequestration and ~9.1×10^{13} kg CO_2 for Mg, Fe, and Ca sequestration, which correspond to 14% and 39% of the amount of atmospheric CO_2 that would return us to 350 ppm CO_2, Thus the CRO, while not capable of eliminating enough CO_2 to halt global warming by itself, still can sequester a considerable amount and should be considered a viable option for mineral sequestration.

Acknowledgements

Many thanks go to my advisor and mentor, Dr. Dawn Cardace, for her insight, advice, breadth of knowledge, endless encouragement, and for having faith that someone with no geology background that is five years removed from school could be a competent graduate student. Thank you to the rest of my committee, Dr. Brian Savage, Dr. Arthur Spivack, and Dr. Mark Stolt.

Thanks also are extended to the McLaughlin Natural Reserve and in particular Cathy Koehler and Paul Aigner for allowing us access to their resources and land. Without their aid and assistance, our project would have been nearly impossible.

Additional thanks to the Rhode Island Space Grant, NASA Astrobiology Institute, and the College of Environment and Life Sciences, for their generous funding of travel, equipment, and research costs.

Thanks are also due for all of the members of the CROMO team: Dr. Matt Schrenk, Dr. Thomas McCollom, Dr. Tori Hoehler, Mike Kubo, Dr. Sanjoy Som, Dr. William Brazelton, and Katrina Twing. You are all brilliant and it was inspiring to be in your company.

Many thanks to my fellow graduate students, especially Laura Schifman, whose Excel and Word expertise and advice all helped through tough times. Thanks also to Ashley McCann, your field assistance and company in the field made 95° F slightly more bearable.

Finally, thank you to my parents. Your support, financial and otherwise, made this entire opportunity possible.

Preface

This thesis is in manuscript format and has been prepared for publication in the journal *Chemical Geology*, but has not yet been submitted, and all formatting has been adapted to the specifications of that journal. Certain undeclared chapters and sections will be used in publication, however at the time of the completion of this thesis, those specific parts are unknown.

Table of Contents

List of Figures

List of Tables

1. Introduction

Warm Earth surface temperatures rely on a functioning planetary greenhouse, and CO_2 is a powerful gas component of this greenhouse. Industrial fossil fuel burning has increased atmosphere CO_2 dramatically in recent times: atmospheric scientists measured atmospheric carbon dioxide levels since 1958 and found that atmospheric CO_2 concentrations have increased since then reached a record high 396.78 ppm in May of 2012, as of the latest Mauna Loa Observatory readings (NOAA-ESRL, 2012). With global temperatures having already risen 1.4°F since the start of the 20th century, and with temperatures likely rise at least another 2 °F—and possibly more than 11 °F— over the next 100 years, the level of CO_2 in the atmosphere is a serious concern (NAS, 2008).

With global population and industrialization increasing, CO_2 levels are unlikely to drop in the near future. The Intergovernmental Panel on Climate Change (IPCC) has modeled possible future atmospheric CO_2 concentrations based on scenarios where certain variables such as population, renewable energy sources as a percentage of total energy, affluence, energy demands, and economic output are altered. Emissions could reach as high as 80 Gt C/yr by 2058 if no action is taken (Mathez, 2009). Both CO_2 levels and global temperatures could reach levels high enough to cause negative impacts on people, agriculture, and wildlife across the world (Fig. 3) (Smith et al., 2009; Thornton, 2012; Doney et al., 2012). The El Niño Southern Oscillation affects ecosystems, agriculture, freshwater supplies, hurricanes and other severe weather events worldwide and is a temperature-sensitive phenomenon, and while it is unclear as to the effects increased temperature will

have (Collins et al., 2010), increasing the risk of permanently changing the way those natural systems function could be perilous.

1.1 Carbon Sequestration Fundamentals

Carbon sequestration occurs naturally and is responsible for moderating carbon dioxide levels in the atmosphere over geologic time. An enormous reserve of carbon is stored in sediment and rocks in the Earth: Ruddiman (2001) estimates 66 million Gt of carbon are stored in sediment and rocks in the Earth. Pre-industrial levels of atmospheric carbon are estimated to be about 600 Gt. Plainly, if the Earth did not have a way to fix carbon dioxide, atmospheric levels would be orders of magnitude higher (Ruddiman, 2001).

Natural sequestration of carbon begins with carbon dioxide in the atmosphere dissolving in the ocean, and is effected through chemical precipitation of carbonate minerals (often biologically mediated) and subsequent compaction into limestone, and/or deposition of mineralized carbon in organic-rich sedimentary shales, the largest reservoirs of carbon on Earth. In natural waters, the speciation of CO_2 is pH-dependent. At low pH values (<6.4), dissolved CO_2 or carbonic acid, H_2CO_3, is the dominant species (pK_H = 1.5 at 25°C). At intermediate, near-neutral pH values, bicarbonate, HCO_3^-, dominates (pK_1 = 6.3 at 25°C). The carbonate ion, CO_3^{2-}, dominates at elevated pH (pK_2 = 10.3 at 25°C) (Fetter Jr., 1980). The carbonate system modulates global biogeochemical cycles in the ocean

and in reactive rock environments, providing essential dissolved inorganic carbon to the biosphere.

Carbon is also naturally stored in plant remains that have been buried and preserved over time to become coal, oil, and natural gas. While the quantity of carbon stored this way is volumetrically subordinate to the carbon stored in limestone, it represents the portion of carbon that is currently being re-released into the atmosphere.

Carbonation of mafic and ultramafic rocks on the Earth's surface occurs naturally as well, locking carbon in geological formations over deep time. Natural carbonation of basalt consumes $\sim 1.8 \times 10^8$ tons of CO_2 per year globally, and is quite a rapid process (Matter and Kelemen, 2009). In Oman, $\sim 10^3$ tons of CO_2 km^3/yr are estimated to be consumed by peridotite carbonation occurring in naturally exposed mantle units of ophiolites (Matter and Kelemen, 2009). Given increased (and increasing) CO_2 generation from anthropogenic sources, the rates of natural sequestration reactions are not sufficient to stabilize Earth's rising temperature.

Human-facilitated carbon sequestration methods include (a) subterranean burial of biomass or biochar (*i.e.,* charcoal created by pyrolysis of biomass), (b) ocean storage of biomass, where biomass is transported down rivers and buried where the river meets the sea (Strand and Bedford, 2009), and (c) injecting aqueous CO_2 below the Earth's surface to be locked in place by carbonation reactions. Iron fertilization of nutrient-limited patches of the global ocean surface has been considered as a means of stimulating primary production (thus drawing down atmospheric CO_2), but the practice could be ecologically disruptive, and models have

consistently shown that at the limit, the approach could not substantially change the trajectory of global warming (Strong et al., 2009). Mineral sequestration has both the largest potential for storage and the lowest potential for CO_2 leakage among sequestration methods (Herzog, 2009), and is the focus of this study.

The largest ongoing mineral sequestration operation is the Carb Fix project in Iceland (Gislason et al., 2010). The project captures CO_2 emitted from the nearby Hellisheidi geothermal power plant and combines it with water to create a carbon-rich fluid. The fluid is then injected into boreholes anywhere from 200 m-2000 m deep, where it reacts with calcium-rich basaltic rocks to form calcium carbonate ($CaCO_3$) (Gislason et al., 2010). Iceland is located on a divergent plate boundary and is composed almost entirely of basalt. As a mafic rock with abundant divalent cations, basalt presents an excellent opportunity for *in situ* capture and storage. Assuming 10% porosity of the rocks, of which only 10% will eventually be filled with calcite, 0.01 km^3 volume is available for calcite precipitation. This volume can accommodate 12 million tons (1.10×10^{10} kg or 10.9 Mt) of CO_2. At the present CO_2 emission rate of magmatic CO_2 from the geothermal power plant at Hellisheidi Iceland (60,000 tons/year), it would take about 200 years to fill this available pore space (Gislason et al., 2010).

However, there are currently no mineral carbon sequestration facilities in the United States, yet ample opportunity exists. For example, the Central Atlantic Magmatic Province (CAMP) — located off the eastern U.S. coast— is partially suboceanic continental flood basalt stretching from Newfoundland in Canada down to Florida (Goldberg et al., 2009). With such an expanse of flood basalt existing

below the ocean, the CAMP presents an opportunity for mineral sequestration using CO_2 dissolved in seawater.

A serpentinite-based mineral sequestration project is being planned in New South Wales, Australia by the GreenMag Group and the University of Newcastle. Because of the lack of suitable geology for deep injection of fluids, the group plans to construct a mineral sequestration plant that takes advantage of the abundance of serpentinite rocks and soils in the area. Plans are underway for its construction, and with a fledgling carbon tax law, there is economic incentive. The successful operation of this plant would provide empirical proof that serpentinite-hosted carbon sequestration is a viable method of carbon capture (GreenMag Group media release, 2010).

In the United States, numerous teams are engaged in research evaluating mineral sequestration in serpentine- and olivine-rich matrices. The Albany Research Center in Albany, OR has conducted research on serpentine and olivine-based mineral sequestration and proposed that moderately high temperature (185 °C for olivine) carbonate mineralization reactions spurred in olivine-bearing rock can convert between 49% and 91% of gas phase or aqueous CO_2 to carbonate mineral phases (O'Connor, 2001).

On the west coast of the United States, continental ultramafic serpentinites and some olivine-rich rocks stretch from Oregon to central California, with enormous potential for carbon storage. These rocks are in close proximity to cities with high populations--San Francisco, Oakland, Sacramento, Napa, Fresno, and San Jose. These cities all demand resources such as electricity, fuel, and cement, all of

which are high-volume CO_2 emitters. Additionally, oceanic crust off the Atlantic and Pacific coasts is broadly suitable for seabed carbon sequestration projects, as described theoretically in Kelemen and Matter (2008) and Goldberg et al. (2009). Xu et al. (2004) state that aquifers containing 'basic' silicate minerals with a high proportion of Mg and Ca, such as olivine, serpentine, pyroxenes and plagioclase, have the greatest potential to fix CO_2 as carbonate minerals because they have a high molar proportion of divalent cations and they react rapidly to form carbonate minerals.

In the following work, I synthesize new data for serpentinite rock cores with regional data pertinent to ultramafic rock characteristics, to quantify the total carbonate sequestration potential of the Coast Range Ophiolite in northern California. Cored rocks comprise two, 31 m and 46 m-deep serpentinite sections, and data include lithostratigraphic columns descriptions, petrography of thin sections, x-ray diffraction results, and bulk and spot solid geochemistry data obtained through x-ray fluorescence (XRF) and scanning electron microscopy coupled to energy dispersive x-ray spectroscopy (EDS). These results will anchor quantitative modeling of the carbon storage possible in these rocks. Recent progress in ultramafic rock carbonation reactions provides context for this study, enabling assessment of Coast Range Ophiolite serpentinites as geological repositories of carbon; Coast Range Ophiolite ultramafic rocks may well represent a significant carbon sequestration option for northern California and serve as a model for other locations.

1.1.1 Carbon Sequestration Chemistry

In the presence of CO_2-rich fluids, with certain temperature and pressure conditions, the following minerals react predictably to from new carbonate minerals (O'Connor, 2005). Note Eq. 1 also involves serpentinization of olivine into serpentine ($Mg_3Si_2O_5(OH)_4$.

$$2Mg_2SiO_4 \text{ (forsteritic olivine)} + CO_2 + 2H_2O \rightarrow Mg_3Si_2O_5(OH)_4 + MgCO_3 \quad (1)$$

$$Mg_2SiO_4 \text{ (forsteritic olivine)} + 2CO_2 + 2H_2O \rightarrow 2MgCO_3 + H_4SiO_4 \quad (2)$$

$$Mg_3Si_2O_5(OH)_4 \text{ (serpentine)} + 3CO_2 + 2H_2O \rightarrow 3MgCO_3 + 2H_4SiO_4 \quad (3)$$

$$Fe_2SiO_4 \text{ (fayalitic olivine)} + 2CO_2 + 2H_2O \rightarrow 2FeCO_3 + H_4SiO_4 \quad (4)$$

$$CaSiO_3 \text{ (wollastonite)} + CO_2 + 2H_2O \rightarrow CaCO_3 + H_4SiO_4 \quad (5)$$

These are simplified reactions. In reality, the process from ore mineral to carbonate mineral contains multiple steps. The primary step is the dissolution of gaseous carbon dioxide into the aqueous phase via

$$CO_{2\,(g)} + H_2O_{(l)} \rightarrow H_2CO_{3\,(l)} \rightarrow HCO_3^-{}_{(aq)} + H^+_{(aq)} \quad (6)$$

The second step is the dissolution of the primary cation reactants from the mineral lattices into solution. The following reaction depicts the dissolution of serpentine from Krevor and Lackner (2011) and olivine from O'Connor et al. (2005).

$$\frac{1}{3}Mg_3Si_2O_5(OH)_{4\,(s)} + 2H^+ \rightarrow Mg^{2+} + \frac{2}{3}SiO_{2\,(aq)} + \frac{2}{3}H_2O_{(l)} \quad (7)$$

$$Mg_2SiO_{4\,(s)} + 4H^+ \rightarrow 2Mg^{2+} + H_4SiO_{4\,(aq)} \quad (8)$$

With aqueous bicarbonate and magnesium ions, the final step of the carbonation reaction is ready to proceed.

$$Mg^{2+} + HCO_3^- \rightarrow MgCO_{3(s)} + H^+ \quad (9)$$

The magnesium and bicarbonate ions react to form magnesite and a proton. The reaction in Eq. 9 will obviously not proceed unless protons are consumed. Proton consumption conveniently takes place during magnesium dissolution in ultrabasic rocks, as seen in Eqs. 7and 8. Thus we have a multi-step process for the carbonation reaction, with a natural proclivity— in ultramafic rocks— to proceed to the right. This is another reason ultramafic rocks are idea candidates for carbon sequestration.

2. Geologic Setting

The Coast Range Ophiolite (CRO) — the oceanic basement beneath the Jurassic and Cretaceous sedimentary rocks of the Great Valley sequence— is an assemblage of ultramafic, mafic, and minor felsic igneous rocks of Jurassic age scattered in a 700 km long segment (Fig. 4) in Northern California (Shervais, 1985; Bailey, 1971). An ophiolite is a section of oceanic lithosphere that has been uplifted

and exposed above sea level and often emplaced onto continental crustal rocks. Geochemical evidence indicates that the CRO formed in a supra-subduction zone. Shervais et al. (2004) propose that the Coast Range Ophiolite formed in multiple stages, beginning with mantle melting at a nascent subduction zone. Further melting induced increased fluid flux from the subducting slab, creating an assemblage of wehrlite and feldspathic peridotite born from refractory melt. As time progressed, the subduction zone matured and stabilized, underlaying the refractory rocks with calc-alkaline and tholeiitic rocks. Finally, the incomplete ophiolite sequence was underthrust by sheet basalts from the subduction of a nearby spreading center. As the spreading center subducted, the leading slab detached and sank into the mantle. When the tailing slab of the spreading center entered the subduction zone, sediments were scraped off, forming an accretionary wedge (the Franciscan Complex, in this case). The newly formed accretionary wedge provided enough buoyant force to uplift and expose the overlying ophiolite sequence (Shervais et al., 2004). Presently, both obduction and accretionary uplift are plausible sources of CRO emplacement.

Ophiolites expose rocks that are stable kilometers below the ocean floor to shallow crustal, continental environments. When basalts, pyroxenites, and peridotites are exposed to water at elevated temperatures and pressures, either through hydrothermal fracturing, convergent margin volatile cycling, or post-emplacement weathering, the pyroxene and olivine in those rocks may be transformed into serpentine minerals. As this is the scenario for the creation of the

Coast Range Ophiolite, outcrops of the CRO comprise: mantle peridotite, gabbro, pyroxenite, basalt, and serpentinite.

3. Methods

3.1 Equipment Used

3.1.1 X-Ray Powder Diffraction

A Terra Field Portable XRD/XRF Instrument (University of Rhode Island) was used to determine the mineralogy of the core samples. The Terra is designed for powder diffraction, requiring that rocks be pulverized before analysis. At least 15 mg of a sample is crushed and sieved to a grain size of 150μm or less, then transferred to the sampling cell. The Terra uses a cobalt anode with 30 kV x-ray tube voltage and 10W x-ray tube power, with the x-ray energy range varying from 3-25 keV. Laboratory default parameters for the instrument are set for 250 exposures, producing both x-ray diffraction (XRD) patterns for mineral characterization and x-ray fluorescence (XRF) spectra for summary geochemical data.

The diffraction patterns are analyzed using XPowder (http://xpowder.com/) software, which compares the diffraction pattern against a database of known mineral patterns and attempts to match based on peak location d-spacings. The user can decide to keep the match or search for specific minerals to attempt to make a match themselves.

Core samples from the field site were generally clay, cobbles, or veins within the cobbles. Isolated samples of each (clay, cobbles, and veins) were run to ensure accuracy of identification of each sample and then a larger sample of cobbles

entrained in clay is run to estimate each constituent. At least one sample from each section of core (a core section is approximately 1 m in length) was sampled, and in the case of a noticeable change in mineralogy, multiple samples from a single core may have been obtained. The corresponding depth and depth interval of each section was noted and a core log was compiled.

3.1.2 Thin Section Petrography

Thin sections were made of a number of cobbles and solid intervals within the cores. Thin sections were cut at the Spectrum Petrographics facility (a fee-for-service lab, petrography.com) and analyzed using an Olympus BH-2petrographic microscope, utilizing both plane- and cross-polarized light. Fields of interest identified via petrography were further studied with a scanning electron microscope.

3.1.3 Energy-Dispersive X-ray Spectroscopy

Thin sections were further analyzed on the JEOL 5900 SEM at the Environmental Scanning Electron Microscope facility in [University of Rhode Island]. Geochemical mapping of points (or tagging) and lines across thin section

surfaces were performed on a portion of a sample to determine elemental abundances within individual crystals or within the groundmass of the slide.

3.1.4 X-Ray Fluorescence

A Thermo Scientific Niton XL3 Series XRF Analyzer was used to determine elemental abundance within each sample. One sample from each core interval was taken. The elements used for analysis are as follows: Zr, Sr, Rb, Pb, Zn, Ni, Co, Ca, Fe, Mn, Cr, V, Ti, K.

3.2 Quantifying Carbon Sequestration Potential

A reasonable quantification strategy takes into account the reactive components in the country rock, available rock volume, and reasonable reaction rates under environmental conditions.

Abundant divalent cations can bind with carbonate anions to form carbonate minerals (O'Connor et al., 2005). O'Connor et al. 2005 suggested the use of a simple equation to develop a 1st order notion of the potential of carbon storage of a system:

$$R_{CO_2} = \frac{100}{(\sum Ca^{2+} + Mg^{2+} + Fe^{2+})MW_{CO_2}} \quad (10)$$

where R_{CO2} is the mass ratio of rock or mineral necessary to convert a unit mass of CO2 to the solid carbonate, *MW* is the molecular weight of the CO_2, and $\Sigma Ca^{2+} + Fe^{2+} + Mg^{2+}$ is the sum of the molar concentrations for the specified cations. The carbonation potential is defined here as the mass ratio of rock or mineral necessary

to convert a unit mass of CO_2 to the solid carbonate. Thus a low R_{CO2} is preferable to a higher one (O'Connor et al., 2005). As a result, minerals with relatively high wt% of Ca^{2+}, Fe^{2+}, and Mg^{2+} are preferred. Typically the silicate anion (SiO_4^{4-}) makes up the majority of the remaining mass of ultramafic rocks and in serpentinized rocks OH^- layers add additional mass from hydration reactions. A list of some ultramafic minerals and their elemental constituents is found in Table 1.

The R_{CO2} equation (Eq. 10) is a deliberate oversimplification of the carbon sequestration potential of any mineral, providing a first order estimate. The minerals in which the cations are bound are important as well; more strongly held Mg, Fe, or Ca ions will require more energy to liberate.

Accurate estimation of the volume of ultramafic rocks in the Coast Range Ophiolite (CRO) is not simple since the CRO is present in many disparate sections, but this is a necessary step in calculating total carbon sequestration potential. Wakabayashi and Dilek (2000) quantify the length of the of the CRO as 900 km, with most outcrops not exceeding 10 km in length, and with an average depth of 5 km. If the CRO were to occupy all of this land, we could constrain a maximum volume as a simple $l \; x \; w \; x \; d$ calculation, to set a maximum volume of 4.5×10^4 km^3. If we compare the idealized maximum area of 9000 km^2 to a map of the Coast Range (Fig. 4.), we can see that ultramafic rocks certainly do not span its entire length and width—thus 9000 km^2 is an overestimation, but provides a working estimate for a maximum possible area.

An ArcGIS-facilitated area estimation of CRO serpentinite better quantifies the serpentinite extent. Through ArcGIS, it is straightforward to sum the areas of each individual rock type on the USGS geologic map of California (Fig. 7). The total area of serpentinites determined in this way is 3865 km^2. Given this area and an average depth of 5 km, the approximate volume of the CRO is 19,000 km^3; this volume is used below as the basis for the carbonation calculation.

3.3 Uncertainty

The calculations made in this paper were based either upon data obtained from previous works or from data obtained from work done specifically for this thesis. There is variable uncertainty with each component used to calculate total sequestration potential, including rock volume, rock density, olivine:serpentine percentage, and magnesium percentage of olivine.

The volume of the CRO contains uncertainty more in the depth component of calculating volume than area. The area component was obtained using reliable GIS data from USGS, while depth was obtained from Wakabayashi and Dilek, (2000). The value of 5 km depth from Wakabayashi and Dilek (2000) was the only source that provided a depth for the Coast Range Ophiolite. As such, it is subject to question, however, it falls within acceptable values for ophiolite depths and will be used despite the inherent uncertainty. Thus, values for depth were chosen using 5 km as a median for the calculations in tables 22 and 23.

Density of the ophiolite was chosen based on known densities of peridotite and serpentinite. Olivine, the primary component of peridotite, has a density of 3300 kg/m^3 and serpentine, the primary component of serpentinite, has a density of 2700 kg/m^3. Values were chosen for density bracketed by the density of olivine and the density for serpentine. The uncertainty of density originates in the uncertainty contained in determining the olivine % of the ophiolite. As the percentage of olivine increases, the density also increases.

The olivine proportion of serpentinite was taken from Choi et al. (2008). Choi et al. (2008) provided % olivine and % serpentine for various sections along the entire length of the CRO. Two outliers were eliminated and the remaining values were assessed. Kelemen and Matter (2008) cited 30% as the amount of peridotite remaining in the Semail Ophiolite. The values of Choi et al. (2008) converged on 38%, thus to continue with estimating conservatively, 30% was chosen as a median value for the calculations in tables 22 and 23.

The magnesium content of olivine crystals was measured by energy dispersive spectroscopy (EDS). The values obtained were then averaged and that value was used in calculating sequestration potential. The value obtained via EDS (24.4% Mg) was lower than what Choi et al. (2008) had reported (29% Mg) for the Del Puerto Canyon portion of the Coast Range Ophiolite, however, Choi et al. (2008) had dunite data for only one portion of the CRO. Thus 24.4% Mg was chosen as a median value for the calculations in tables 22 and 23, since the aim of this paper is to achieve a conservative estimate.

4. Results and Discussion

Carbon sequestration rate and total potential are dependent on a number of factors: most fundamentally, available carbon dioxide and free reactive cations, (*e.g.,* Mg^{2+}, Fe^{2+} and Ca^{2+}) are necessary. CO_2 can be readily dissolved in a manufactured fluid, naturally occurring groundwater or seawater. Sufficient cations result from alteration of ultramafic rocks. Sequestration also responds to pressure-temperature conditions, mineralogy, rock chemistry, porosity/permeability, and solution chemistry. Each of these items impacts net carbon sequestration and affects calculations of the total mass of carbon that can be fixed through the idealized reaction of Coast Range Ophiolite ultramafic rocks.

It is important to note that the sequestration outlined in this paper is not that of drawing CO_2 out of the atmosphere to reduce atmospheric CO_2 levels, but rather delineating the CRO as a repository for sequestering future carbon emissions. Drawing CO_2 out of the atmosphere in an attempt to reduce atmospheric levels of would be unfeasible, as the amount of time it would take to accomplish the level of sequestration desirable would be overwhelmed by the amount of CO_2 generated by human input during that time. Thus, "sequestration" in this sense could more accurately be worded as "storage," however , the term "sequestration" has historically been used to convey what "storage" entails.

4.1 Temperature-Pressure Constraints on Carbonation Reactions

Like most processes in nature, carbonation of olivine and serpentine are both greatly aided by the presence of heat. Heating the rocks is a necessary step, as the carbonation reaction is slow at lower temperatures. Natural carbonation occurs wherever there are mafic and ultramafic rocks exposed to either atmospheric or dissolved CO_2. Kelemen and Matter (2008) showed that $4x10^7$ kg yr^{-1} of CO_2 are sequestered in this manner every year at the Semail Ophiolite. While that is an impressive figure, that rate needs to increase by orders of magnitude to use mineral sequestration as a primary carbon dioxide mitigation process. O'Connor et al. (2005) showed that olivine reacts most ideally at 185 °C and 150 atm P_{CO2}, whereas serpentine requires a costly 600 °C preheating procedure that costs too much money and energy to be considered useful. The rate of CO_2 sequestration can be elevated to as high as an estimated $2x10^9$ tons of CO_2/km^3 per year (Kelemen and Matter, 2008).

Thus, olivine rocks should be preheated with hot fluid before they are reacted with any CO_2. Fortuitously, the carbonation reaction is exothermic, so the reaction of creating carbonate minerals (Eq. 9) can generate enough heat to sufficiently warm the surrounding rocks and aid in boosting the reaction kinetics to keep carbonation reactions continuous and rapid and to prevent the constant need to heat and pump non-CO_2 fluid down into the borehole. With the aid of heat pretreatment and increasing the partial pressure of CO_2 in solution, rates can be increased anywhere from 10^6 to 10^9 times the natural rate (Kelemen and Matter, 2008).

4.2 Serpentinite and Peridotite Mineralogy

Minerals in mafic and ultramafic rocks (*i.e.*, rocks rich in magnesium and iron compared to silica) provide cations necessary for mineralization of carbonate. The most common mafic minerals include olivine, pyroxene, serpentine, and amphibole. Wollastonite ($CaSiO_3$), olivine (Mg_2SiO_4) and serpentine [$Mg_3Si_2O_5(OH)_4$] are the best candidate minerals for carbon sequestration (O'Connor et al., 2005; Matter and Kelemen, 2011). However, serpentine>>olivine>wollastonite in terms of abundance at Earth's surface, (O'Connor et al., 2005), underscoring the interest in serpentine as a candidate mineral reactant.

4.2.1 Constituent Minerals

Serpentinite minerals that figured prominently in XRD and petrographic findings are discussed briefly below:

Magnetite is a common accessory mineral in serpentinites. Its presence can be explained via the oxidation of iron(ii) hydroxide:

$$3Fe(OH)_2 \text{ (iron(ii) hydroxide)} \rightarrow Fe_3O_4 \text{ (magnetite)} + 2H_2O(l) + H_2(g) \quad (11)$$

where the iron(ii) oxide originates from the serpentinization of olivine:

$$5Mg_2SiO_4 \text{ (forsterite)} + 9H_2O(l) + Fe_2SiO_4 \text{ (fayalite)} \rightarrow 3Mg_3Si_2O_5(OH)_4 \text{ (serpentine)} + Mg(OH)_2 \text{ (brucite)} + 2Fe(OH)_2 \text{ (iron(ii) hydroxide)} \quad (12)$$

(Schulte et al., 2006).

or by:

$(Mg,Fe)_2SiO_4 + nH_2O + CO_2 \rightarrow Mg_3Si_2O_5(OH)_4 + Fe_3O_4 + CH_4$ (13)
(Oze and Sharma, 2005).

under CO_2-rich conditions, such as might be expected in submarine serpentinization, or a shallow crustal continental setting with active meteoric water inputs.

Olivine (Mg_2SiO_4) is the predominant mineral in peridotite, which comprises the bulk of the Earth's upper mantle. Olivine is one of the two minerals—the other being pyroxene—that commonly transforms into serpentine minerals via exposure to water, heat, and pressure.

Albite ($NaAlSi_3O_8$) is a common igneous and low grade metamorphic mineral. It is the most sodic form of plagioclase. The albite in the Coast Range Ophiolite region originates from oceanic crust portion of the ophiolite, which is composed mostly of basalt (Shervais and Kimbrough 1985). Albite is also a common mineral found in greenstones, basalts that have undergone low-grade greenschist facies metamorphism at temperatures between 300 and 450 °C and pressures of 1 to 4 kbar (Deer et al., 1992). Many of the rocks in the CRO have been subject to hydrothermal alteration under greenschist facies pressure/temperature conditions (Shervais and Kimbrough 1985). In the landscape, more weather-resistant greenstones protrude from the surrounding serpentine. The basalt, greenstone, and serpentinized peridotite occur together in a regional-scale mélange (Shervais and Kimbrough, 1985), and also intermix sporadically in the cores examined here.

Clay and clay minerals: The clay mineralogy of weathered serpentinites is complex. The heterogeneity of serpentinite textures—mesh, hourglass, blade (Wicks and Whittaker 1977)—and the occurrence of additional rock-forming minerals, like chlorite, add to the complexity of the system (Caillaud et al., 2006). It is not uncommon to see saponite, nontronite, montmorillonite, or vermiculite. The XPowder XRD database does not have a nontronite or a saponite reference file, however XRD data show multiple peaks consistent with the presence of montmorillonite and/or vermiculite. In the CRO, smectites are a result of serpentine weathering and are represented in all tables in this paper as "clay". Vermiculite indicates weathering of chlorite, which occurs in each core also. Often both clay minerals are mixed together, and their diffraction peaks overlap, so it is difficult to parse which mineral is present.

Tremolite ($Ca_2Mg_5Si_8O_{22}(OH)_2$) is an amphibole mineral that occurs in low-grade metamorphic ultramafic rocks and is a common accessory mineral for serpentinites (Deer et al., 1992). It is also a regular component of greenstones and as such only occurs in the core samples when other greenstone minerals are present. Tremolite alters to talc, chlorite, and carbonate minerals, depending on geochemical context (Deer et al., 1992).

Calcite ($CaCO_3$) is a product of the calcium-rich and carbon-poor groundwater coming into contact with carbon dioxide either from the atmosphere or from meteoric water. Veins of calcite are strewn throughout the core samples, a result of hydrothermal precipitation of waters enriched in calcite via meteoric influx.

Lizardite $(Mg,Fe)_3Si_2O_5(OH)_4$ is a polymorph of serpentine and is produced through alteration of olivine and pyroxene. It is the lower temperature and pressure phase of serpentine polymorphs (Moody, 1976). It is impossible to discern antigorite from lizardite in a hand sample, so x-ray diffraction must be utilized. Even with XRD, it is not entirely clear which polymorph is present. XRD most strongly supports the presence of lizardite.

4.3 Core Descriptions of Serpentinites from CROMO1 and CROMO2

One or more samples were taken from each core section. Interval sizes are irregular as a result of incomplete core collection, different sized core inserts during drilling, and occasions when auger drilling with no sample retrieval were necessary.

4.3.1 Summary Stratigraphy: CROMO1

0-1.98 m: The first 1.98 m of the Core Shed Well is a soil layer near the surface and records intense biological, physical, and chemical weathering. The bulk composition of this soil is magnetite-rich clay with albite and quartz, most likely from the weathering of nearby greenstones (Fig. 8). Albite is one of the primary minerals composing both basalts and greenstones. When basalt is metamorphosed to greenstones, some minerals get chloritized. Further erosion of chlorite can produce vermiculite (Caillaud et al., 2006), which is suggested by XRD data but would require further testing to confirm.

1.98-2.44 m CROMO1 1,5 represents the first strong presence of lizardite (Fig. 9) and additionally the end of any evidence of bioturbation (e.g., the first 20 cm contain roots, however no signs of flora or fauna exist beyond the first 20 cm). Core samples have a fine-grained clayey matrix with angular clasts. XRD determined the clay is composed of primarily lizardite and the clasts are greenstone, composed primarily of albite with minor chlorite.

2.44-4.57 m. This horizon nearly mimics the topsoil in terms of mineralogy, but shows increasing lizardite (Fig. 10). Cores consist of rounded clasts (sand- to pebble-sized), in a muddy clay matrix. Separate samples of the clay yield evidence of both serpentinite and greenstone minerals along with clay minerals. Clasts of both serpentinite and of greenstone are dispersed throughout the clay.

8.61-12.65 m A mélange of serpentinite, greenstone, and clay minerals continues, with a distinct tremolite signature (Fig. 11), which differentiates this interval from the 2.44-4.57 m horizon. One section of CROMO1-13 is covered by a white rind that effervesces when reacted with HCl; thus it is carbonate-rich. The peak does not show up definitively in XRD as there are too many other mineral phases (XRD noise) represented. Most clasts range from coarse sand to coarse pebbles. Drilling may have broken up larger weathered cobbles of serpentinite.

12.65 - 27.43 m Greenstone minerals tremolite, chlorite, and albite are absent for the next 15 meters. There is a predominance of lizardite and magnetite (Fig. 12)

with some clay (Fig. 13). Lizardite is not in solid cobbles, but rather large, intact, amalgamated pieces that appear to be massed together from tectonic activity; quite possibly the cores sample a shear zone and this is representative fault gouge material. Samples from this site are very friable, with clay intruding where some of the lizardite is schistose with stacked and separated phyllosilicate layers.

27.43 - 31.09 m Greenstone and serpentine mix as large cobbles and intact core segments. Hand samples are denser than pure serpentine and lack the greasy luster and platy qualities of serpentine hand samples. Petrography reveals abundance of twinned plagioclase crystals (Fig. 14), which is supported by XRD (Fig. 15). Since entire cobbles from this horizon show concurrent greenstone and serpentinite, it can be attributed not to the mixing of horizons from tectonism, but rather from partial serpentinization during the metamorphosis of basalt to greenstone. Additionally, there was a vein of calcite in this section at 27.5 m depth, which was isolated and analyzed (Fig. 16). Recall that calcite formation is a result of the natural carbonation process that ultramafic rocks undergo.

4.3.2 Summary Stratigraphy: CROMO2

0.00-1.37 m The topsoil layer is composed predominantly of lizardite and magnetite present in friable pieces situated in a yellow-brown lizardite clay (Fig. 17). Plant roots are present throughout, though less so than at CROMO1. CROMO2 area is considerably drier, so the top soil is not as moist and is more oxidized than CROMO1 (Fig. 18).

5.03 – 22.86 m This interval contains an extensive segment of pure serpentinite minerals, with a predominance of lizardite and magnetite and little to no clay minerals or greenstone minerals. There is an exception occurring at 6.10m depth, where there is a small pocket of greenstone clasts (Fig. 19) fragmented along with lizardite clay (Fig. 20). Aside from this interval, the specimens appear identical in hand sample and contain angular pebble-sized lizardite clasts in light grey clay (Fig. 21).

22.86 – 25.91 m This interval displays an extremely strong clay mineral signature with a slight lizardite and magnetite presence (Fig. 22). Individual clasts within the clay matrix register as clay minerals as well, possibly montmorillonite.

25.91 – 36.58 m The mineralogy in this interval signifies a return to the mineralogy seen in horizon 18.08-22.68 m. Serpentinite and greenstone mineral assemblages (Fig. 23) are present in friable, loosely compacted cobbles and small angular clasts, respectively. The cores from this sample are very muddy and very dark in color. Within the mud, there are greenstone and serpentinite clasts (Fig. 24) that appear black with traces of dark green, along with schistose green and white serpentinite masses (Fig. 25).

36.58 - 45.72 m The deepest CROMO2 interval contains pure serpentinite minerals. The diffractogram pattern shows prominent sharp peaks for lizardite and magnetite (Fig. 26). The rocks from this interval were harder than the overlying schistose rocks. The hardness of the rock from enabled us to make thin sections of a few of the

sections. The thin section images enforce what the XRD data showed, in terms of mineralogical content (Figs. 27 and 28)

The cores from this interval appear far less weathered and the presence of clay and clay minerals is largely absent. Serpentinite is present as friable but intact material, with a small layer of hard serpentinite cobbles (Fig. 29) at CROMO2-136 at 44 m depth. Though the mineralogy does not change in this interval, there is variance in color and rock habit throughout. The topmost 3 m of this layer consists of a very hard dark green serpentinite that is not friable like most of the serpentinite seen in other core samples; the serpentinite is together in solid hard pieces. There is then a transition to a light brown and green serpentinite (42.5 m) that becomes more friable with increasing depth, and ultimately the core ends with a very dark green and black sample of serpentinite of intermediate hardness. CROMO drilling ceased here, so for deeper data, we must rely upon previously drilled holes and data in the literature.

Prior to the 1980s, when the Homestake Mining Corporation surveyed the land that is now the McLaughlin Natural Reserve, a series of strategically placed holes were drilled to focus gold-mining activities in nearby silica-rich hydrothermal deposits. These exploration-related cores remain intact, and one deep serpentinite core was sampled for thin section review. The drill site for this core was destroyed during gold mining activities, but was located <5 km to the SE of the CROMO drilling location; this site will for simplicity be called Homestake Mine Pit Borehole (HMPB), and the depth of the sample is about 110 m below the surface.

4.3.3 Deep Core Specimen- Homestake Mine Pit Borehole

Homestake Mine Pit Borehole (HMPB), ~110 m depth: This core sample is very hard and shows no signs of friability or schistosity. The sample resembles hard serpentine in hand sample, and while subtly different in texture, does not appear different from shallower cored sections until examination with petrographic microscope. Fig. 30 shows that strongly birefringent olivine is present (note blues, pinks, purples, yellows, and oranges) and there is also a large pyroxene crystal in the NE corner of the slide with streaks of serpentine running through it. Both the olivine and the pyroxene have been serpentinized to some degree [serpentine minerals and magnetite are scattered throughout the thin section field of view], however much less so than in shallower rocks.

4.3.4 Integrated View of CRO Subsurface Rocks, McLaughlin Locality

Overall, the shallowest 45 m of CRO rock at McLaughlin show nearly complete serpentinization. In addition to serpentinite rocks, there are greenschist facies rocks distributed throughout the cores. Often, greenschist facies rocks (here taken to be metamorphosed mafic igneous rocks containing chlorite, albite and tremolite among other phases) occur in a sample of core alongside serpentinite minerals, with the close juxtaposition of phases a result of the history of repeated convergent margin tectonism in northern California. Peridotite with relict olivine grains does not occur in the shallowest rocks, but does indeed present at 110 m depth (Fig. 30). Between 45 m and 110 m, the mineralogy may shift gradually from

more to less serpentinized, or there may be a contact zone of some kind (not detected in cored samples) that causes a sharp transition; only further coring or comprehensive access to archived cores with Homestake will determine the nature of the transition. Presently access to Homestake cores is limited due to a building structure safety issue where they are being housed.

Notably absent from the cores were some of the more common accessory minerals in ultramafic rocks. Talc ($Mg_3Si_4O_{10}(OH)_2$) is often found associated with serpentinization, however, XRD failed to show any significant proof of its presence, perhaps due to a dearth of excess silica during serpentinization or the absence of CO_2 during any metamorphic changes in the serpentine. Also absent from the XRD results is brucite ($Mg(OH)_2$), which forms during the serpentinization of dunites (Deer et al., 1965). It is possible that brucite was once present, but has since been weathered away or dissolved by either meteoric water or groundwater, or is present in such small amounts that it is undetectable by XRD.

Observations of ultramafic rock cores sampled at the McLaughlin Natural Reserve indicate that the peridotite has been heavily serpentinized in general, but that relict olivine and pyroxene grains were present and visible under the petrographic microscope.

4.4 Geochemistry

The mineralogy of a system controls whether it is an effective sequestration vehicle, but geochemical data determine to what degree the host rock will function effectively in sequestration projects. Ultramafic rocks are defined by their mineral content. The adjective *ultramafic* implies the abundant presence of magnesium and iron (recall that magnesium-ferric contracts to mafic) and those elements, along with calcium, serve as the primary cations in sequestration reactions.

While I will concentrate my efforts on olivine only, efforts continue to make carbonation of serpentine a more feasible sequestration option. Park et al. (2003), for example, increased the rate of dissolution of magnesium from serpentine by adding a mixture of 1 vol% orthophosphoric acid, 0.9 wt% of oxalic acid and 0.1 wt% EDTA (ethylenediaminetetraacetic acid); they greatly enhanced the Mg leaching process of ground serpentine while preventing the precipitation of Fe(III) on the surface of the mineral particles (Park et al., 2003). When this acidic solvent was used for the aqueous mineral carbonation, the overall process was limited by the rates of dissolution of CO_2 and dissociation of carbonic acid, rather than the dissolution rate of the serpentine (Park et al., 2003). However, the temperature at which these processes occurred is ~500°C and requires too much energy input to make sequestration a viable option.

In fact, serpentinite-based carbon sequestration has a useful advantage over peridotite-based models in one sense: the carbonation of serpentinite results in considerably less volume change than carbonation of peridotite. Because carbonation of serpentinite results in a smaller volume difference, the chance of

clogging pore spaces is reduced, allowing CO_2-rich fluids to percolate over longer time scales in the subsurface during *in situ* carbonation (Beinlich et al., 2012). Free flow of pore fluids allows the reaction to proceed continuously, though the slow rate of carbonation of serpentinite (Gerdemann et al., 2007) may not result in the generation of sufficient heat, through exothermic reaction to bring the surrounding rocks up to temperature.

The focus here will be on the divalent cation elements in olivine that occur in abundance in ultramafic rocks, *i.e.*, calcium, iron, and magnesium; these elements are particularly good at binding with carbonate anions to form carbonate minerals (O'Connor et al., 2005).

Since the CROMO surface rocks have considerably lower olivine: serpentine ratio and also contain abundant greenstone and clay minerals, they are not ideal for *in situ* carbon sequestration. However, they still have potential as a source for *ex situ* sequestration, whereby the rocks are mined, ground up, heated, and exposed to CO_2-rich fluids and allowed to react. This process is much more controversial, given dollar costs, carbon footprint, and environmental impacts, and is discussed in more detail in section 4.9.1.

4.4.1 Point Geochemistry via SEM-EDS, to Determine Cation Abundances

SEM-EDS was applied to areas of interest on selected thin sections, for which separate mineral phases were analyzed for specified elements. Geochemical data for

the ultramafic mineral phases relevant to carbon sequestration are presented below, as average wt% of each element from multiple samples analyzed.

CROMO2-134, 40 m depth: The serpentine phases from this section average 22.0 wt% Mg and 11.3 wt% Fe and less than 1 wt% Ca (Tables 3 and 5). The serpentine from this interval is in the form of a massive matrix-like lizardite (Fig. 31 and 32) and chrysotile, which grows laterally in vein-like structures (Fig. 31). There is also abundant magnetite scattered throughout the thin section, either as a massive-textured rim-like growth or as octahedral individual crystals (Fig. 31). The magnetite is enriched in iron, with weight percentage averaging 70.4% (Table 4).

CROMO2-136, 43 m depth: The serpentine phases from this section average 22.4% Mg, 10.9% Fe and 0.2% Ca (Table 6). Aluminum in these rocks was extremely low; 0.06 wt% Al was the maximum value obtained. The serpentine phases in this section were predominantly of a massive texture with no evidence any vein-like growths. There were two scant magnetite crystals as well (Fig. 33), but they were not analyzed for elemental abundance.

Homestake Mine Pit Borehole (HMPB) at 110 m depth: The thin section from HMPB shows a different mineralogy. As in the petrography image, there are far more pyroxene than olivine crystals. This thin section provided geochemical data for deeper CRO olivine and pyroxene phases, yielding valuable insight into the sequestration capability of the CRO rocks.

Six fields of view were examined via SEM-EDS. The first region of interest (ROI) contained a sample of pyroxene amid a groundmass of serpentine (Fig. 34). The serpentine was of massive texture and was likely lizardite. The geochemical make-up of the serpentine phase was lower in magnesium (18.4%) and higher in calcium (1.33%) and iron (12.4%) than any of the previous serpentine samples (Table 7).

Pyroxene is visible in two different ROI (Figs. 34 and 35). The pyroxene in Fig. 34 contains a crystal displaying parallel cleavage planes, with ongoing serpentinization around and within the crystal. Of the common ultramafic minerals, pyroxene minerals (including wollastonite and diopside) typically contain the highest calcium wt% (Table 2). The pyroxene crystal analyzed here had higher calcium (22.3%) than any of the serpentine or olivine minerals analyzed. The crystal from the ROI in Fig. 34 also showed minor amounts of iron (3.9%) and magnesium (7.4%) for a total divalent cation percentage of 33.6%. The crystal in Fig. 35 was thoroughly fractured but lacked cleavage. Elemental abundances for the Fig. 35 pyroxene show slightly lower Ca (20.5%), but higher Mg (8.5%) and Fe (4.5%). However, the amount of calcium in the grain is still significantly higher than any other mineral phase. Pyroxene with this proportion of minerals relates most accurately (Fig. 40) to diopside ($MgCaSi_2O_6$), thus it is taken to be the dominant pyroxene present in the CROMO1 and CROMO2 cores. Olivine was also present in this slide and can be seen in the ROIs in Figs. 36 and 37. Olivine is represented in the ROI in Fig. 37 as four scattered and fractured crystals amid massive lizardite and streaks of magnetite. The olivine from the ROI in Fig. 36 contains a higher

percentage (Table 12) of magnesium (24.5%) than any of the other mineral phases present in any of the ROI. The olivine from the ROI in Fig. 37 contains less Mg (Table 13) than the portion of olivine sampled from Fig. 36, and has relatively the same concentration of Mg as the serpentine phases sampled from all depths.

The other ROI of the slide from Fig. 37 and the other prevalent mineral phase in the HMPB slide is a spinel group mineral enriched in iron, chromium, magnesium, and aluminum (Tables 14, 15, and 18). The spinel began as chromite ($FeCr_2O_4$) and due to ion replacement, a ferritchromite rind forms that is completely devoid of aluminum (Ulmer, 1974). As mineral assemblages alter, iron may also be concentrated in magnetite (Fe_3O_4), which tends to form rims around the ferritchromite rinds (Ulmer, 1974), which can be seen in the CRO rocks (Figs. 38 and 39). As a result, the spinel takes on the characteristics of a zoned crystal, with chromium and aluminum concentrated in the center and, iron and chromium on the inner edge, and iron with little to no aluminum or chromium on the outer edge (González-Mancera et al., 2007).

Iron and magnesium are both mobilized in the course of serpentinization; the inventories of these elements are lower in the serpentine phase products than they are in the initial olivine phase. During serpentinization and carbonation, minerals with higher Mg# (*i.e.,* nMg/(nMg+nFe), where n is number of moles)) than parent olivine and pyroxene are formed (Evans 2008) thus lowering the concentration of Mg in the olivine and pyroxene phases. These minerals include serpentine, talc, dolomite, magnesite, and calcite. Formation of high Mg# minerals increases the total

amount of mobile iron in the system; excess iron is typically taken up in oxide and hydroxide minerals including goethite [FeO(OH)], brucite [$(Mg,Fe)(OH)_2$], hematite [Fe_2O_3], and magnetite [Fe_3O_4]. Among these iron-rich oxyhydroxides, a preponderance of magnetite occurs relative to the other minerals in the rocks at the McLaughlin locality (see section 4.3.1).

Table 19 shows the average weight percentages for serpentine, spinel, olivine, and pyroxene present in the CRO rocks analyzed in this work. The elemental concentrations of the rocks closely resemble the predicted values from Table 2. Serpentine minerals had higher average (over 3%) Mg and slightly lower than average Fe. Olivine had lower than expected Mg and higher than expected Fe. Pyroxene contained minor amounts iron and aluminum; however this cation replacement alters the percentages of magnesium and calcium.

4.4.2 Bulk Solid Geochemical Data from X-Ray Fluorescence

Additional geochemical data was obtained for samples from CROMO1 and CROMO2. The XRF unit operated under atmospheric pressure rather than under vacuum, thus concentration data for elements lighter than sulfur including magnesium and aluminum data are absent.

Given the relatively shallow total depth of coring (to only 30 m and 45 m below surface), no strong pattern emerged from calcium or iron data. One core sample per section was analyzed, thus these data should be taken as spot samples of the entire cored volume. The highest concentration analytes were calcium and iron (Tables 3

and 4). Nickel, manganese, chromium, and titanium were also abundant in the cores, with sections of the core often containing 1,000 ppm or more (see tables 20 and 21). A strong potassium signature in the geochemical data matches up with the XRD evidence of greenstone minerals, mirroring K-inventories in altered clay phases. Potassium and sodium often substitute for one another in feldspar minerals, so tracking potassium in the cores could help indicate where greenstone intercalations are likely to be found in a dominantly serpentinitic set of cores.

4.5 Porosity and Permeability Constraints

Maintaining travel paths for the CO_2–rich fluids requires both creation and maintenance of pathways. Opening new pathways is achieved by the precipitation of carbonate: as carbonation proceeds, stress builds up in the host rock (Rudge et al., 2010), and fractures result.

Continuation of the forward reaction must be ensured, sustaining carbonation as long as reactants are available. This would result in fewer drilled holes and lower energy consumption overall, cutting drilling-related CO_2 emissions and total project costs. Ensuring continuation of the reaction requires a continual heat source and open flowpaths (*i.e.*, permeability) through which the CO_2-rich fluid can travel and react with the surrounding rock, as well as ongoing replenishment of CO_2. Furthermore, heterogeneity of the pore structure leads to the establishment of preferential flow paths, which ensure efficient spreading of CO_2-rich fluids throughout the whole sample of rock (Andreani et al., 2009).

Carbonation efficiency can be hindered by the formation of minerals on the surface of olivine grains. Magnetite and/or silica-rich saponite and talc form around the rims of olivine grains, preventing the dissolution of olivine and/or pyroxene. Eliminating the "protective" barrier from the olivine grains is critical to allowing the dissolution reaction (Eq. 14) to progress.

$$Mg_2SiO_4 + 4H^+ \rightarrow 2Mg^{2+} + H_4SiO_4 \text{ (O'Connor et al., 2005)} \quad (14)$$

Curtailing unwanted mineralization on olivine grains is critical. A study by Andreani et al. (2008) showed that silica-rich layers form on olivine grains at the greatest frequency during diffusion-dominated transport of the flowing solution. Diffusion-dominated transport implies that transport is controlled by a concentration gradient and not by advective forces and, as such, is much slower. The reduced speed provides sufficient time for the silica-rich layers to form, enhancing the surface reactions. On the other hand, if flow is advection-dominant (fast), the flowing solution does not have sufficient time to interact with the olivine grain and passes without appreciable dissolution of the olivine grain. Therefore, transport that is both advective and diffusive (*i.e.,* moderate injection rates) should ensure at least partial carbonation of the rock while maintaining reservoir permeability, given that other conditions are met (Andreani et al., 2008).

Lastly, cracking of surrounding rock relies on kinetics. Reactive cracking may be likely during rapid mineral carbonation and unlikely during slow carbonation (Matter and Kelemen, 2009). This notion further supports the use of olivine as the primary mineral reactant, owing to the rapid kinetics of olivine

carbonation (O'Connor et al., 2005). A reaction-driven kinetics model is supported by extensive outcrops of completely carbonated peridotite (listvenite or listwanite) in the Semail Ophiolite in Oman that show that natural carbonation is not always self-limiting (Nasir et al., 2007). Further, Boschi et al. (2009) discovered in Malentrata, Italy, hydraulic fracturing and subsequent magnesite precipitation of surrounding ultramafic rocks helped maintain a high structural permeability during the whole hydrothermal event, creating conduits for the input and output fluids. If the natural processes seen in Italy and Oman can be reproduced, then *in situ* mineral sequestration would hold an even greater advantage over *ex situ* mineral sequestration.

4.6 Solution Chemistry

The final component of the carbonation process is the composition of formation fluids. Supercritical CO_2 would be the most reactive available solution, but obtaining it would be difficult and maintaining a temperature and pressure regime capable of supporting a supercritical state may not be economically feasible. Compressed liquid CO_2 is more feasible, but still requires processing to obtain. Dissolving carbon dioxide into solution is the next best option. O'Connor et al., (2005) conducted a set of experiments designed to determine the optimal combination and concentration of additives to enhance the rate of carbonation.

4.6.1 pH

pH plays a conflicting role in carrier solution chemistry (O'Connor et al., 2005). An acidic solution would better serve a solution targeting olivine dissolution. As can be seen from Eq. (14), a supply of H^+ ions is needed for the reaction to proceed. The reaction for carbonation of Mg^{2+} ions requires a basic solution, however. As in Eq. (15):

$$Mg^{2+} + HCO_3^- \rightarrow MgCO_{3\,(s)} + H^+ \quad (15)$$

For this reaction to proceed to the right, H^+ ions must be consumed, which in a basic solution is accomplished by free OH^- ions that will react as follows:

$$OH^- + H^+ \rightarrow H_2O_{(l)} \quad (16)$$

O'Connor et al. (2005) showed that the addition of sodium bicarbonate ($NaHCO_3$) to the solution reduced the required residence times to achieve a reaction of approximately 80% from 24 hours to 6 hours, while holding all other carbonation constants stable. It was proposed that the addition of $NaHCO_3$ causes the Mg in olivine to interact directly with bicarbonate ions (Eq. 17).

$$Mg_2SiO_{4\,(s)}\ (\text{forsteritic olivine}) + 2HCO_3^- \rightarrow 2MgCO_{3(s)} + SiO_2 + 2OH^- \quad (17)$$

This reaction, which is even more exothermic than serpentinization, is followed by hydroxide interacting with dissolved carbon dioxide to form more bicarbonate.

$$OH^- + CO_{2\,(aq)} \rightarrow HCO_3^- \quad (18)$$

Additionally, O'Connor et al. (2005) found that the addition of NaCl also improved the reaction rate, possibly due to Na^+ ions modifying the surface charge of silicate particles, which expedite ion exchange at the solid liquid interface. Cl^- ions may form complexes with magnesium, further increasing solubility of magnesium in solution (O'Connor et al., 2005); interestingly, regional groundwaters very near the McLaughlin locality exhibit some brine characteristics derived from interaction with local Great Valley sedimentary sequences and could serve as a readily available source of these ions (Goff et al., 2001). In general, the maximum concentrations of $NaHCO_3$ and NaCl found to be soluble in water at ambient conditions are 0.64 M $NaHCO_3$ and 1M NaCl. Overall, there is now sufficient experimental evidence for enhanced carbonation to serve pilot studies in the field in the CRO.

4.7 Calculation of CO_2 Sequestration Potential in the CRO

Using the volume of reactable rock, the mineralogy of the rock, and the chemical compositions of the minerals which compose the rock, the approximate total carbonation yield is calculated here. If the calculation is based solely on the magnesium content of olivine (Goff et al., 2000), a conservative, minimum estimate is reached for the possible amount of CO_2 that can be sequestered. Examples of the calculations involved are provided below (from Kelemen and Matter, 2008).

For example, to calculate sequestration potential using only Mg^{2+}:

With a depth of 5 km, volume: 19,500 km^3 = $1.95x10^{13}$ m^3

Density of partially serpentinized peridotite: 2800 kg/m^3

Calculation for mass of serpentinized peridotite: $1.95x10^{13}$ m^3 x 2800 kg/m^3 = $5.5x10^{16}$ kg

Percentage relict olivine: 30% (Choi et al., 2008; Kelemen and Matter, 2008)

Weight percentage of Mg in olivine: 24.4 wt% Mg

Carbonation rate: 1% carbonation rate (Matter and Kelemen, 2009)

$5.5x10^{16}$ kg ore * 30% * 24.4% * 1%* (44g/mol CO_2 / 24.305 g/mol Mg) = **$7.3 x 10^{13}$ kg CO_2 sequestered or 73000 Mt.** (19)

The sequestration potential of these rocks is increased by including calcium, magnesium, and iron in olivine in the reaction with CO_2. By repeating the same computation for iron and calcium and summing the three figures, it is possible to obtain a total CO_2 sequestration amount, binding all three cations.

$7.3x10^{13}$ kg CO_2 (from Mg) + $1.7 x 10^{13}$ kg CO_2 (from Fe)+ $7.0 x 10^{12}$ kg CO_2 (from Ca) = **$9.7 x 10^{13}$ kg CO_2 total CO_2 or 97000 Mt**. (20)

The difference between using only magnesium and using all three cations is 23,600 Mt of CO_2; this is a large mass of carbon, but within the same order of magnitude. In this particular example, considering iron and calcium results in a 34% increase in the amount of CO_2 sequestered.

Certain variables that factor into sequestration potential impact the estimated potential sequestration quantities to greater and lesser degrees. Figures 41, 42, and 43 display sequestration potential, with variables such as formation depth, formation density, and olivine percentage in the formation being manipulated. Considering a wide range of variables creates a range of possible CO_2 drawdown figures. These figures constrain a most conservative estimate and also allow for a best-possible scenario.

Figure 41 shows sequestered CO_2 mass against density of the formation. Density of the formation affects sequestration potential in that a higher density calculates to a greater mass of reactable rock, which in turn allows for a greater mass of carbonate to form from the rock. Density is primarily dependent upon the mineral composition of the rock. If peridotite is around 30% olivine and 70% serpentine as is the case in the Semail Ophiolite (Kelemen and Matter 2008), and is the ratio I have chosen for the CRO then the density would equate to ~ 2800 kg/m^3.

Figure 42 shows the olivine fraction of the peridotite against sequestered CO_2 mass. Since olivine is the most reactive of the ultramafic minerals (aside from rare wollastonite), a higher percentage of olivine in the rock will increase the sequestration potential of the rock. A study by Choi et al. (2008) showed a wide range of serpentinization of Coast Range peridotite. Some sites were as low as 18% serpentinized and some were as high as 95% serpentinized. An average of all the values acquired from this study reveals a mean serpentinization of 61.5%. The Semail Ophiolite consists of ~30% olivine peridotite (Kelemen and Matter, 2008), so

to again be conservative with estimates, I chose to round the 61.5% obtained from Choi et al. (2008) to 70%, based on review of the new data in this study. I have chosen values as low as 20% and as high as 40% to determine a maximum and minimum percentage of olivine in the CRO rocks.

By considering possible depths to which the Coast Range Ophiolite ultramafic unit extends, I have created a range of volumes for the CRO. A deeper formation simply means more there is more volume and thus more mass of rock to react. Depth is difficult to determine in the formation, as complex tectonism has confounded the determination of depth for each individual portion of the CRO. Wakabayashi and Dilek (2000) provide an average depth of around 5000 m, considered here as a generous estimate. 5500 m is taken as a maximum depth and 3500 m as a minimum depth, so as to err on the conservative side and to recognize the practical difficulty of drilling 5000 m or more.

After all of the possible scenarios were evaluated, the Mg-only case (Table 22) and the Mg+Fe+Ca case (Table 23) are presented. Furthermore, the maximum possible value and the minimum possible value, based on the parameters set forth in this paper, are hereby established—providing extremely conservative and extremely generous estimates for CRO sequestration potential (Table 24). Note that the upper limit of sequestration potential is only 3.6 times greater than the lower limit, showing that even given variability in host rock and cation reactivity, the sequestration potential is in fact fairly well constrained.

The averages obtained are close in value to the calculations shown in (Eqs. 19 and 20). For Mg-only sequestration, a total of 6.8×10^{13} kg CO_2 (6.8×10^4 Mt, 7.5

x 10^{10} tons) is able to be sequestered in the CRO and for Mg, Ca, and Fe, the total amount of CO_2 that can be sequestered is 9.1 x 10^{13} kg (9.1 x 10^{4} Mt, 1.00 x 10^{11} tons). There are currently ~2.9 x 10^{15} kg CO_2 in the atmosphere; if we were to draw down all 9.1 x 10^{13} kg of CO_2, we could eliminate 3.1% of the carbon dioxide in the atmosphere. If only Mg reacted, then 2.3 % of the carbon dioxide could be drawn down.

5.0 Conclusion

The Coast Range Ophiolite, situated along a 700 km stretch in California, provides an opportunity to study and work with highly reactive rocks that are in disequilibrium with surface conditions. I proposed to evaluate the harnessing of this disequilibrium to react the ultramafic rocks with carbon dioxide, in an effort to sequester atmospheric CO_2, as has been proposed as a large scale means of geological sequestration of carbon recently (Kelemen and Matter, 2008; Goldberg et al., 2009; Gislason et al., 2010). Geochemical and mineralogical data enabled calculation of the potential of the CRO rocks for carbon sequestration capability. XRD, SEM-EDS, and petrography determined that surface rocks were rather thoroughly serpentinized, with no visible trace of relict olivine in any of the surface rocks sampled. One deeper serpentinite sample from the vicinity had prevalent olivine and pyroxene. Through the compilation of SEM-EDS mineral geochemistry data, with relevant geochemical data from sources from previous research, the total quantity of CO_2 that may be sequestered in CRO ultramafic rocks was estimated as ranging from 4.60×10^{13} to 1.24×10^{14} kg CO_2. For comparison, Kelemen and Matter (2008) estimated the larger Semail Opholite's potential total drawdown as 6.9×10^{14} kg CO_2.

In all, the quantity of carbon dioxide that can be sequestered in the Coast Range Ophiolite alone is significant. Whether the capacity of the CRO is based on magnesium only (2.3% of atmospheric CO_2) or magnesium, iron, and calcium (3.1% of atmospheric CO_2), the capability of the CRO to serve as a mitigating agent should not be ignored. If we are to return to 350 ppm (as recommended by the IPCC) from

present (as of 1/3/2013) 392 ppm, we would need 11% of the CO_2 currently in the atmosphere to be consumed. This is not to say we are capable of pulling that quantity of CO_2 out of the atmosphere, but rather we are able to sequester a quantity that represents a percentage of current atmospheric CO_2. Industry will continue to produce carbon dioxide, and the best way to currently control emitted CO_2 is to capture and store it, preferably in close propinquity to where it is produced.

Since there are $\sim 2.9 \times 10^{15}$ kg CO_2 in the atmosphere, 3.2×10^{14} kg of that quantity need to be sequestered. The CRO represents 14% (Mg-only) - 39% (Mg, Fe, Ca) of that total, which is insufficient by itself, but represents a significant value for a moderate sized ophiolite.

While serpentinites and peridotites remain compelling as candidate rock hosts for the geologic sequestration of carbon, research regarding their utility in more than experimental scales is still inchoate. Any field-scale test of carbon sequestration potential in the CRO must consider also environmental impact assessments (the protection of rare serpentine endemic eco-systems is of paramount importance), dangers of carbon leakage from an incompletely sealed subsurface reservoir, and net carbon emissions of the entire process, among other concerns. Given the considerable areas of variably altered peridotite in continental and submarine settings, serpentinite-based carbon sequestration would be an enticing mitigation strategy for anthropogenically enhanced atmospheric CO_2 levels, should the reaction conditions and longevity be sufficiently controllable.

Appendix A - Figures and Tables

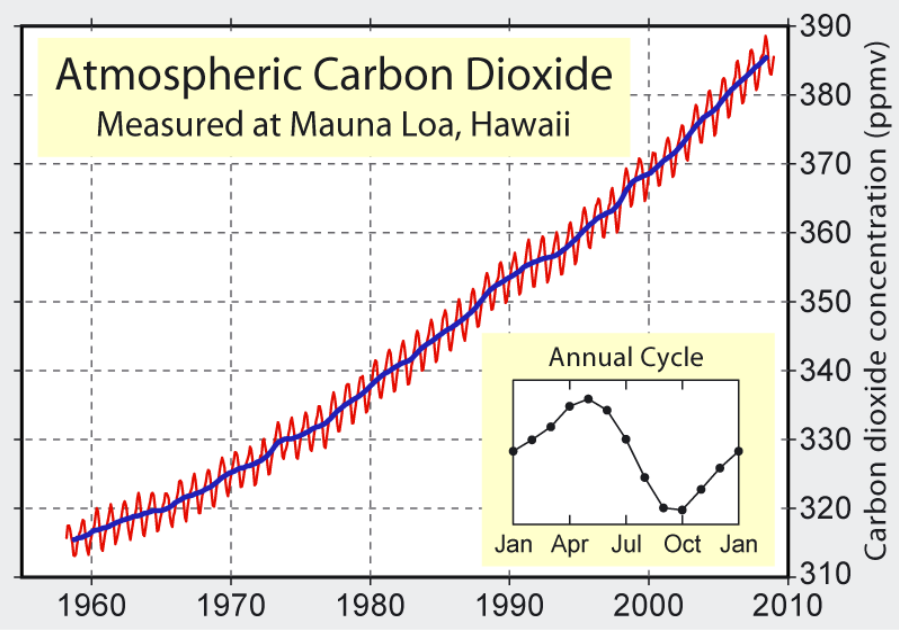

Fig. 1. Graph shows CO_2 levels in parts per million in the atmosphere since 1958. Sawtooth pattern is due to seasonal changes as shown in inset plot at lower right (NOAA 2010).

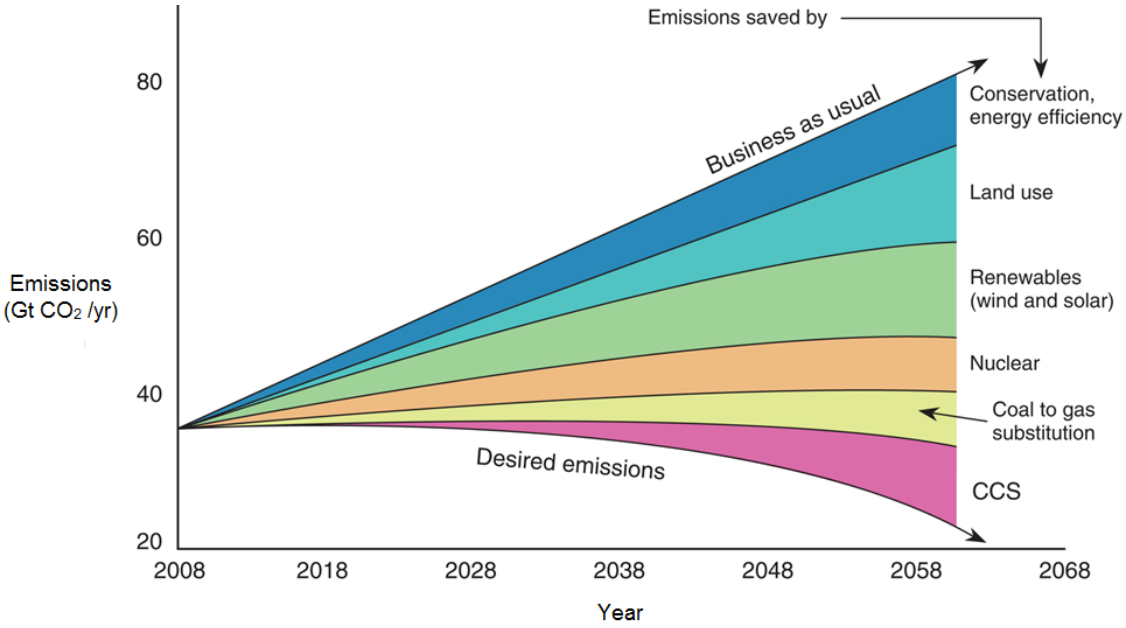

Fig 2. Graph shows possible CO_2 emissions scenarios based on courses of action taken (Mathez, 2009).

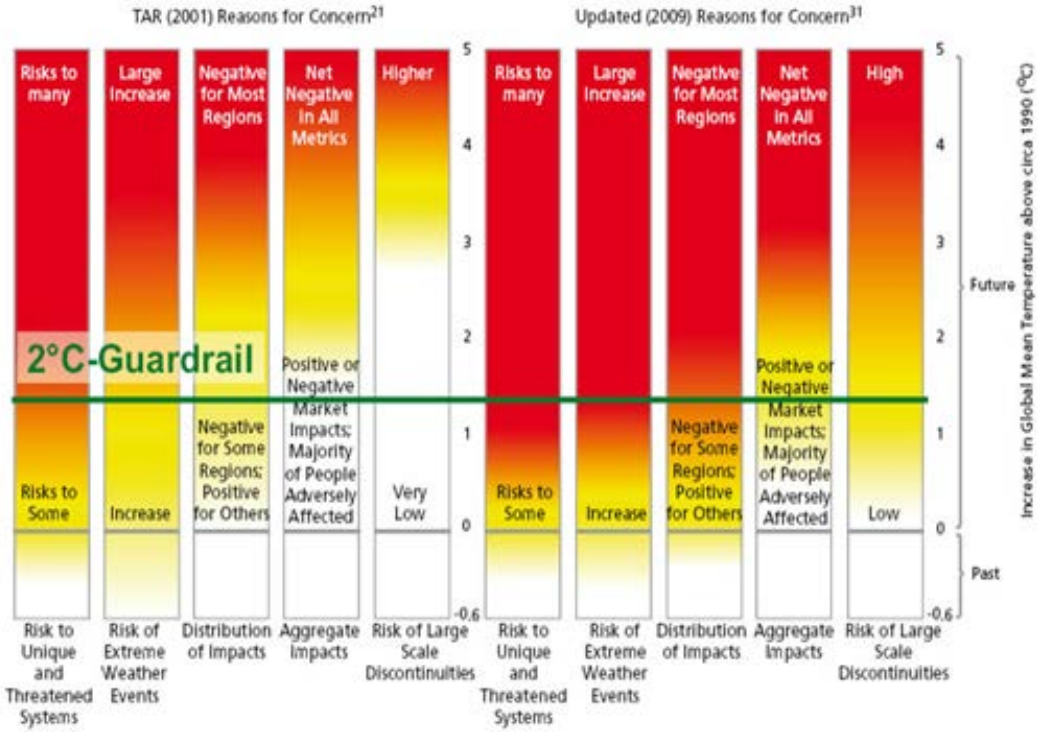

Fig. 3. Burning Embers graph showing probability of side effects with relation to temperature rise (Richardson et al. 2009).

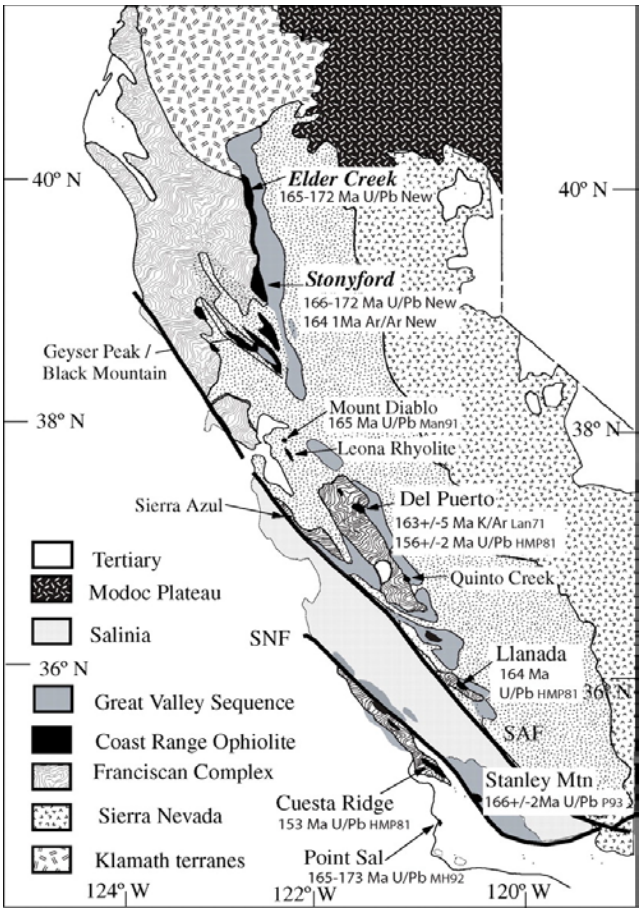

Fig. 4. (Jayko 1987) Map of California displaying presence of select geologic formations: note the Coast Range Ophiolite rocks are solid black.

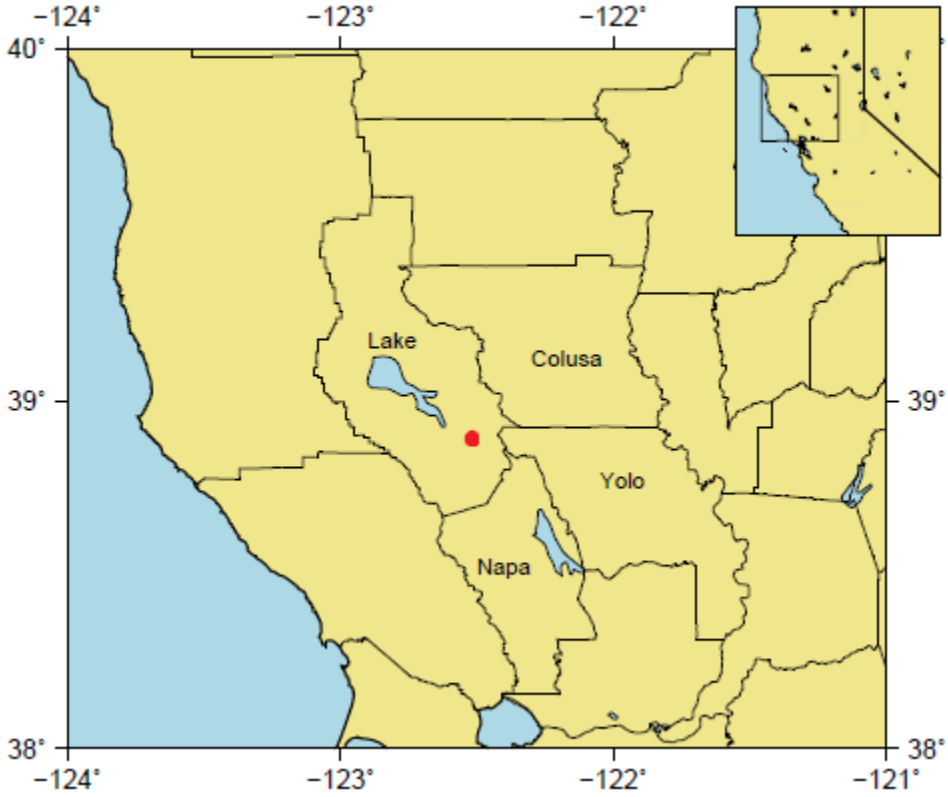

Fig. 5. Map showing location of McLaughlin Natural Reserve (in red) in relation to California.

Fig. 6. Location of CROMO1 (CSW) and CROMO2 (QV) sites on the McLaughlin Natural Reserve (Fig. 5) in Lower Lake, CA.

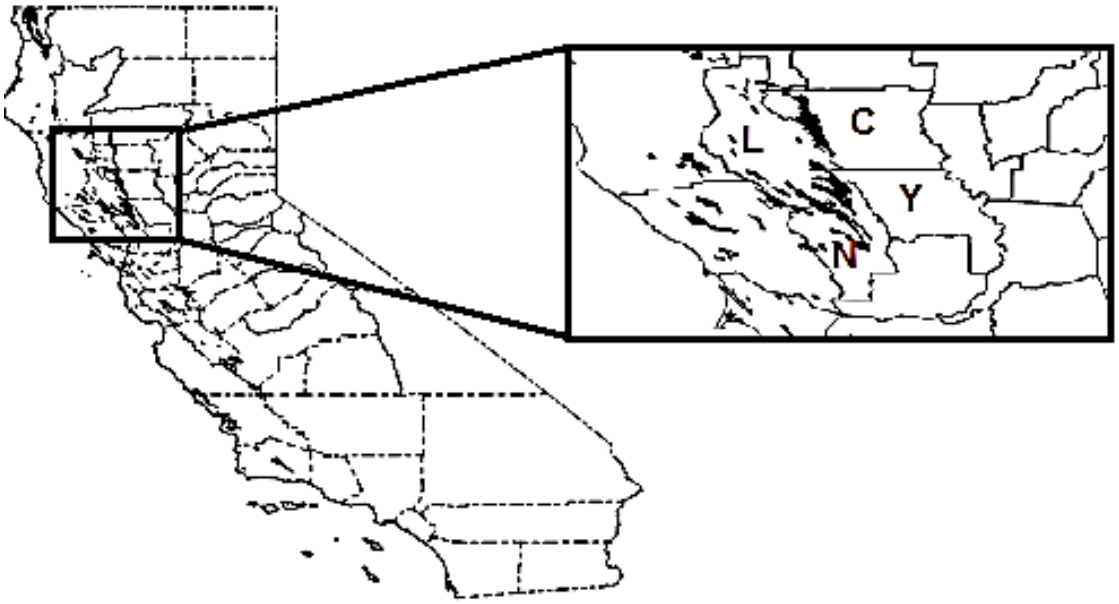

Fig. 7. Map of California displaying serpentinite outcrops in black. Zoomed portion of map focuses on Colusa (C), Yolo (Y), Napa (N), and Lake (L) counties. (Created in ArcGIS 10.)

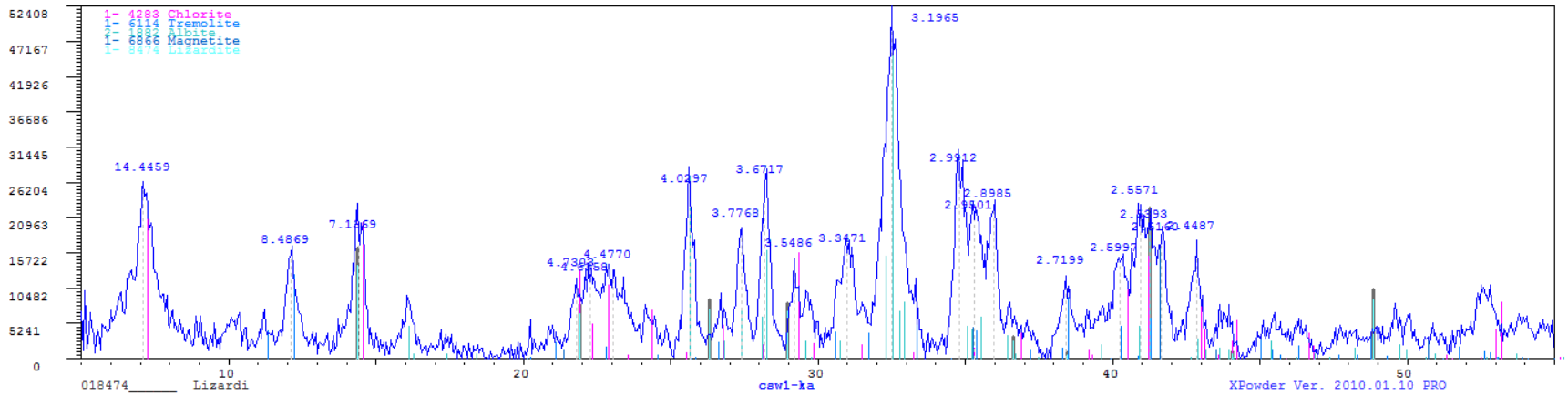

Fig. 8. Diffractogram from CROMO1-1 at 0.45 m depth. The pattern shows frequent peaks at many different intervals implying a very heterogeneous topsoil composition. The predominant minerals are albite (3.1965 Å), chlorite (14.4459 Å, 7.1369 Å, 4.7 Å) and magnetite (2.5571 Å).

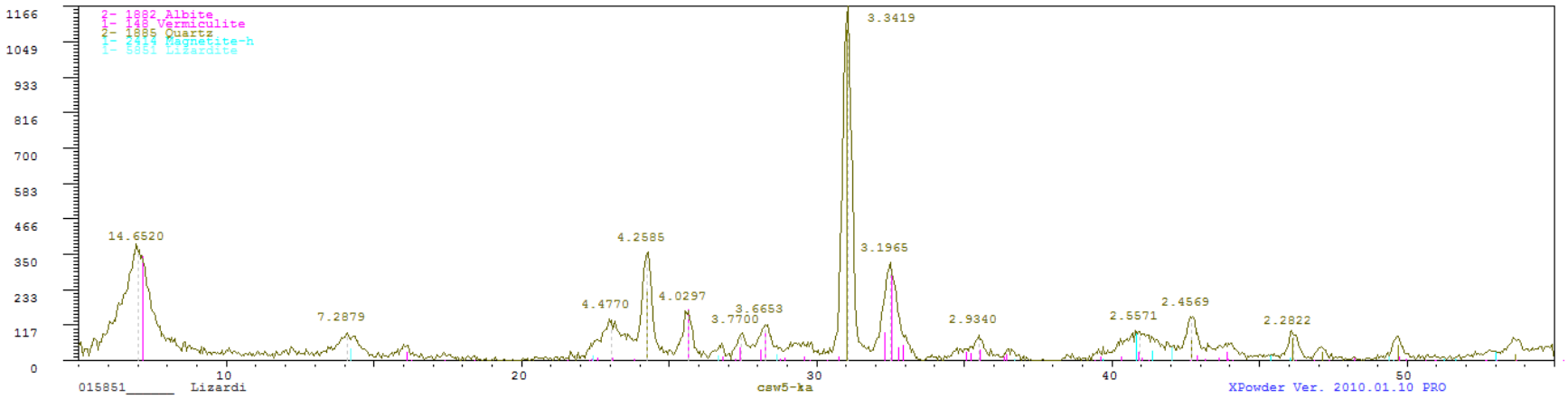

Fig 9. Diffractogram from CROMO1-5 at 2.44 m depth. The peak at 7.2879 Å shows first slight presence of lizardite. High intensity peak at 3.3419 Å represents quartz, likely a product from erosion of greenstones. Evidence of greenstone exists with albite peak at 3.1965 Å. High quartz:albite ratio shows more stable quartz has survived while albite has been broken down over time. The second highest peak is a clay mineral(s) on the left, also indicative of erosion.

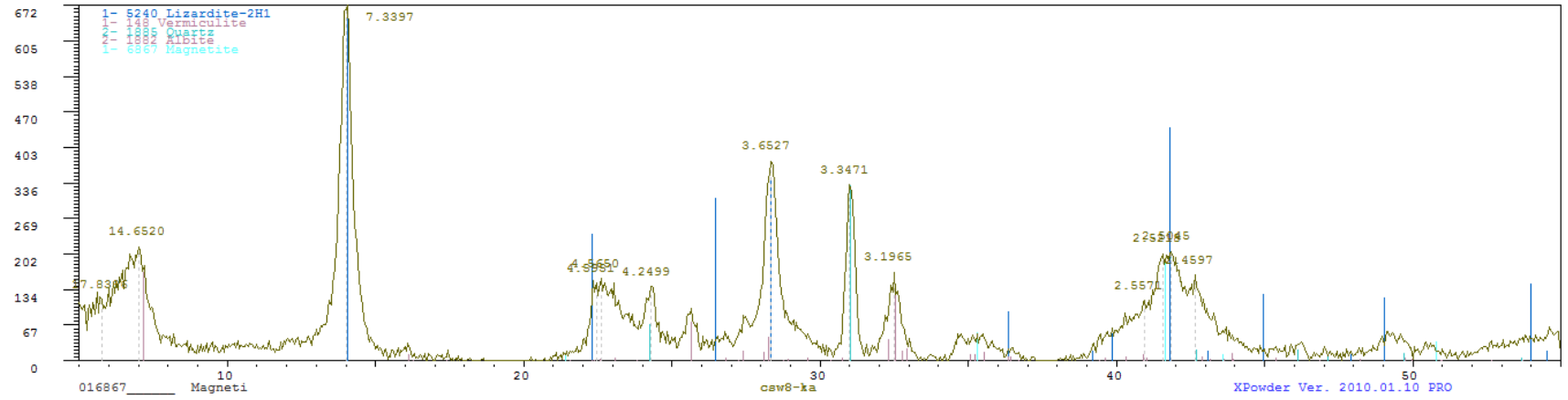

Fig. 10. Diffractogram from CROMO1-8 at 3.96 m depth. There is a lingering presence of albite, quartz, and clay minerals. Lizardite (7.3997 Å, 4.6 Å, 3.6527 Å) replaces quartz as the dominant mineral present. Accessory mineral magnetite surges wherever lizardite surges, affirming their affinity for co-occurrence.

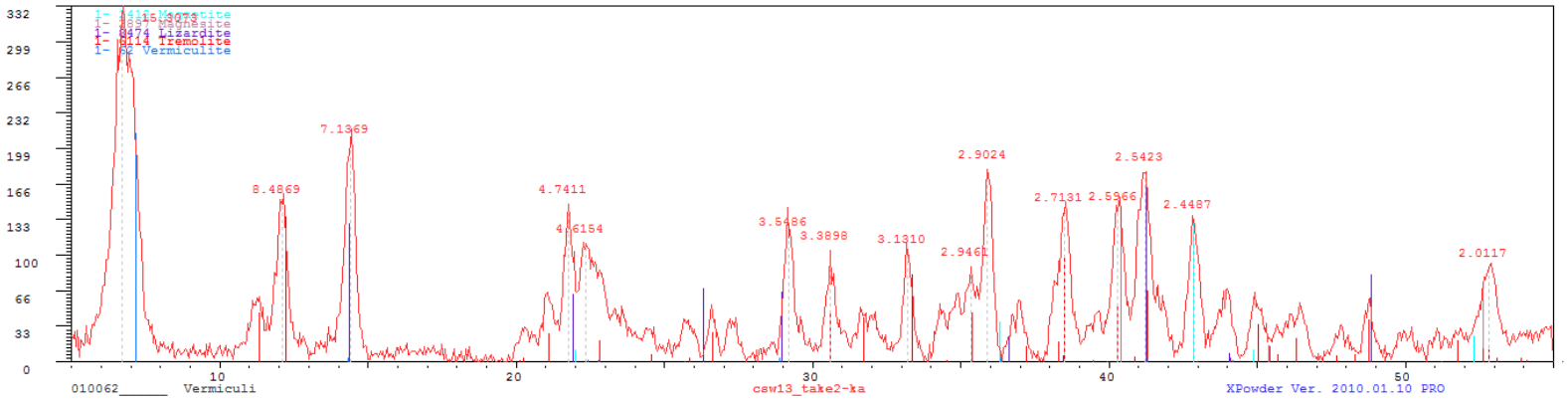

Fig. 11. Diffractogram from CROMO1-13 at 10.74 m depth. Heavy clay presence indicated by highest peaks on far left side with strong tremolite (8.4869 Å, others), lizardite (7.1369 Å, 4.7 Å), and magnetite (2.5 Å) peaks.

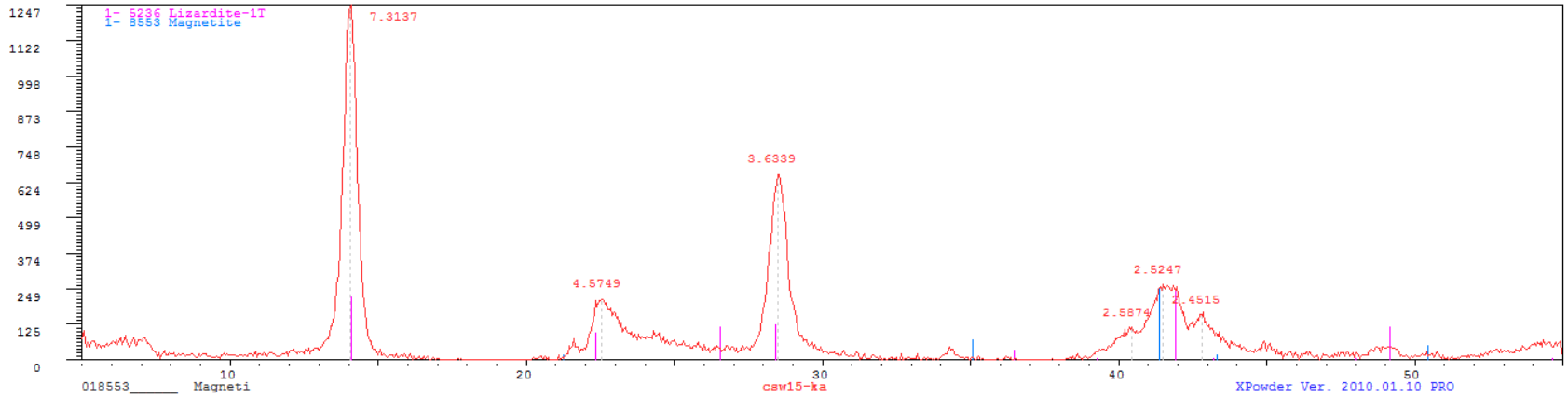

Fig. 12. Diffractogram from CROMO1-15 at 13.82 m depth. Low clay peak (far left) with strong lizardite (7.3 Å, 4.57 Å, 3.6 Å) and magnetite peaks (2.5 Å). Low background noise indicates purity of sample and absence of extensive weathering.

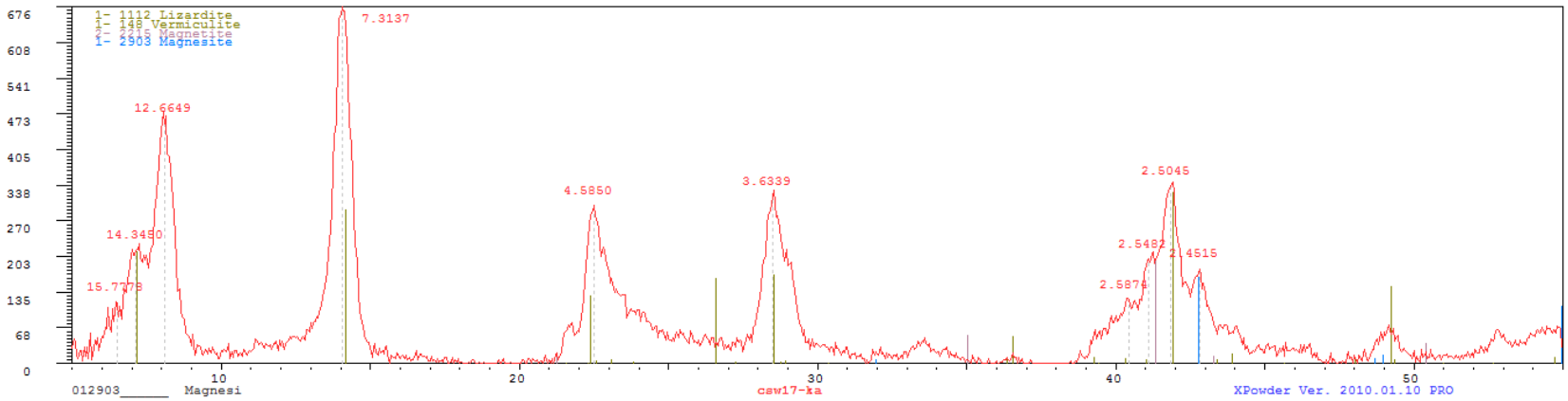

Fig. 13. Diffractogram from CROMO1-17 at 18 m depth. The diffractogram is similar to fig, but with more prominent clay signature. Lizardite (7.3137 Å, 4.5850 Å, 3.6339 Å) and magnetite (2.5045 Å) main peaks remain in high proportion, with some minor magnesite at around 2.4515 Å.

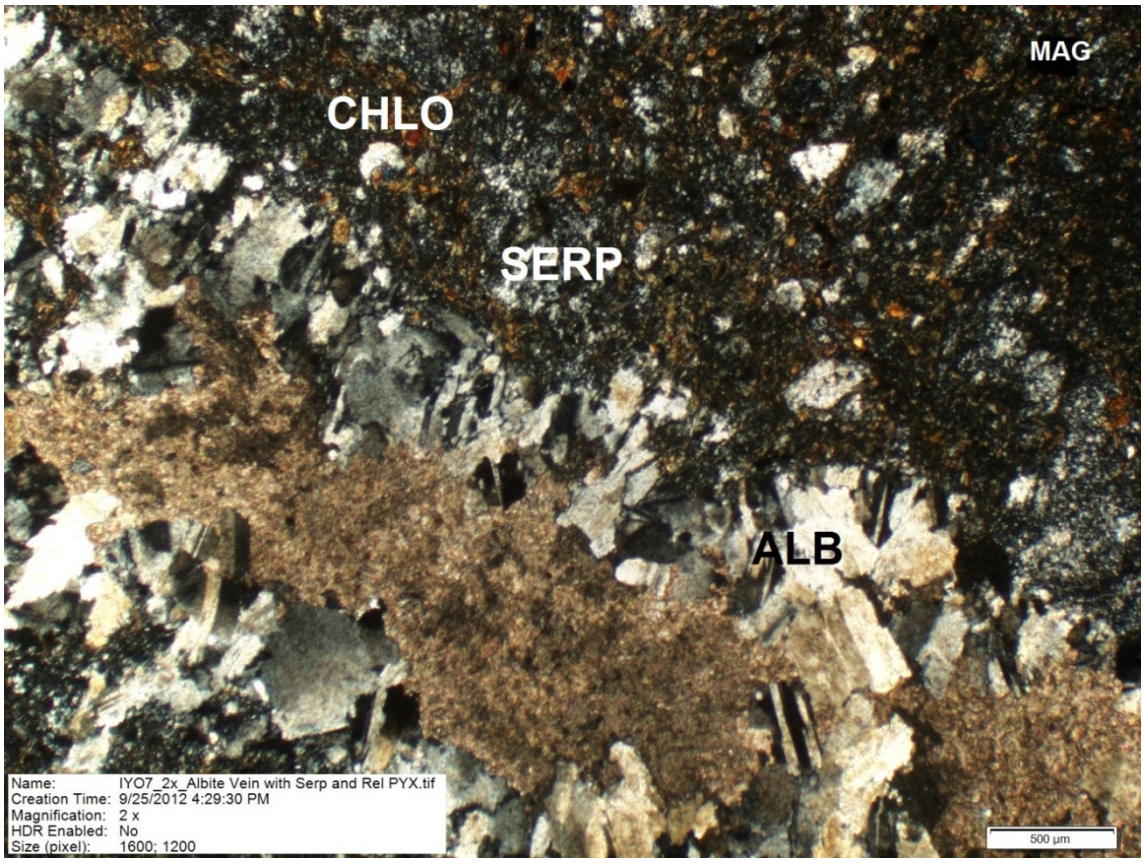

Fig. 14. 2x magnification of a thin section from CROMO1-29 at 31 m depth under cross-polarized light. Albite crystals are the white and black twinned crystals that appear to extrude vein-like diagonally from the SE corner to the NW corner. Serpentine is present as black and white mottled minerals in the N and NE portion of the slide. Chlorite, another greenstone mineral shows up as slightly green-hued under cross polarized light and can be seen pervading the thin section.

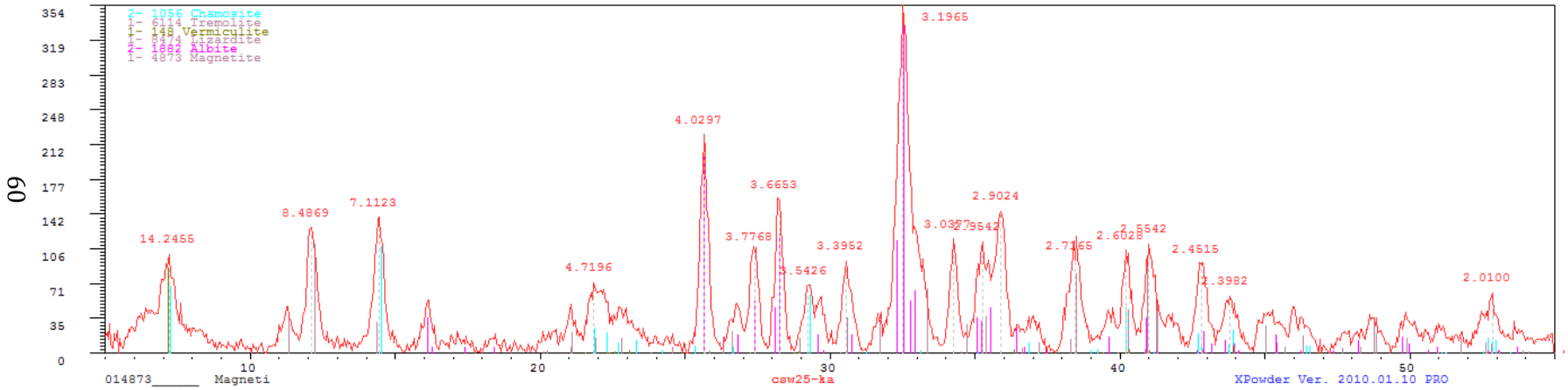

Fig. 15. Diffractogram from CROMO1-25 at 27.97 m depth shows return to greenstone assemblage preponderance (albite (3.196 Å), tremolite (8.48 Å, other minor peaks), chamosite (14.25 Å, other minor peaks) with minor amounts of lizardite (7.1 Å, 4.7 Å) and magnetite (2.45 Å) as well as clay mineral (14.2 Å) peaks.

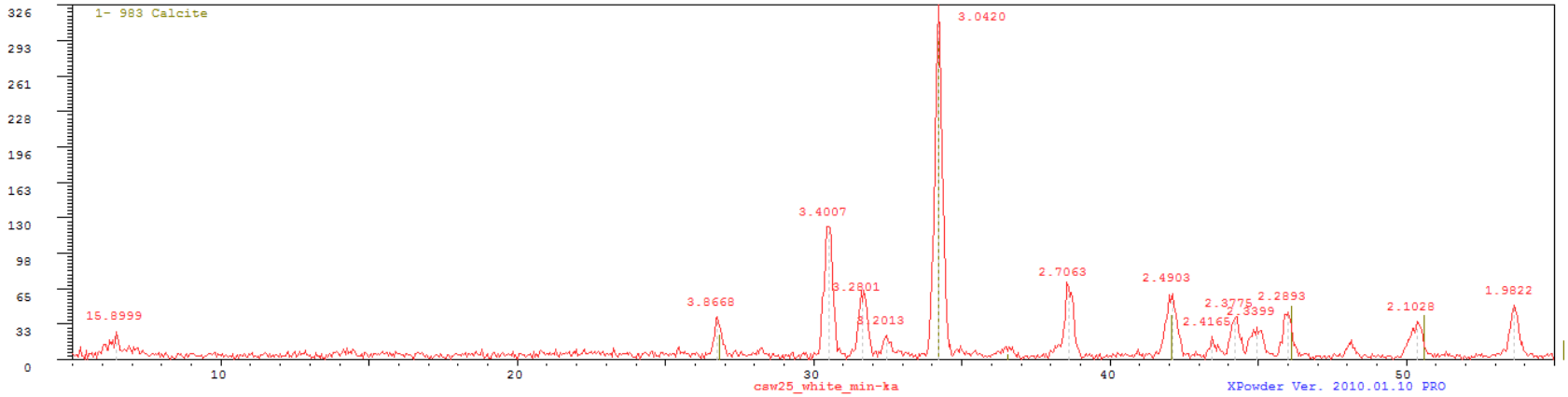

Fig. 16. Diffractogram from CROMO1-25 at 27.5 m depth showing major peak of calcite with other minor unidentified minerals.

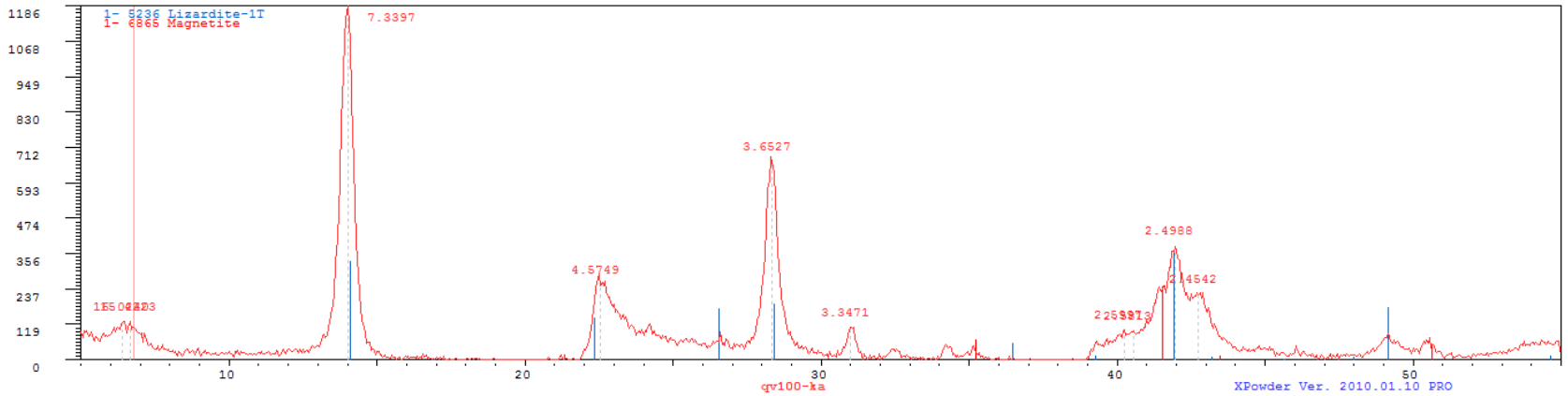

Fig. 17. Diffractogram from CROMO2-1 at 0.45 m depth. The topsoil is very magnetic and is composed almost entirely of magnetite (2.5 Å) and lizardite (7.3 Å, 4.5 Å, 3.6 Å) with some minor peaks around quartz (3.3 Å) and clay minerals on the far left.

Fig. 18. Core taken from first 0.9 m of CROMO 2, essentially equivalent to serpentine-dominated valley topsoil. Photo credit: A. McCann.

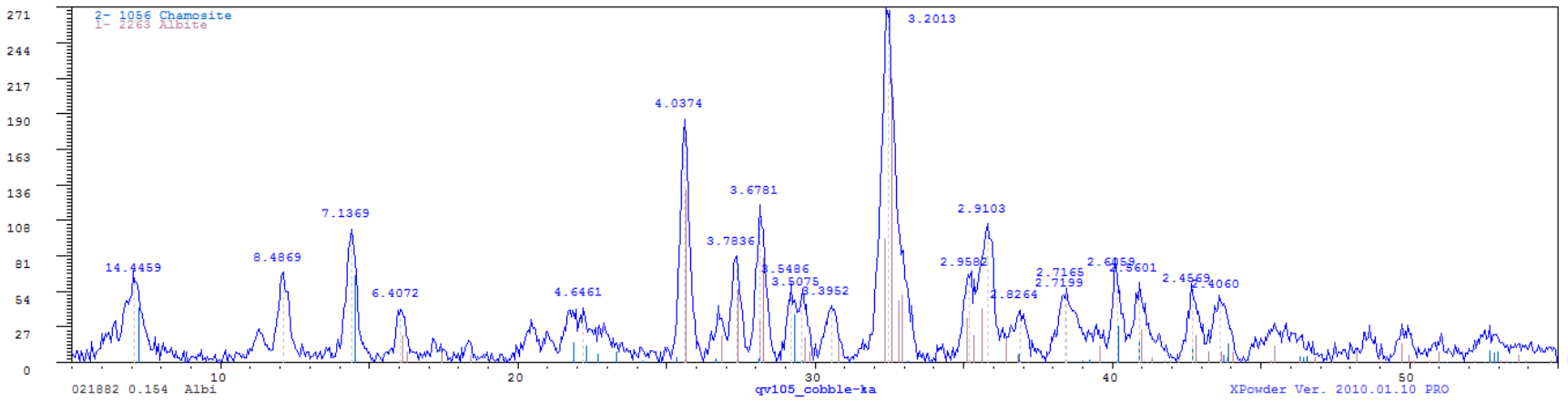

Fig. 19. Diffractogram of an individual clast from CROMO2-105 at 6.10 m depth. The greenstone minerals chamosite (Fe-end chlorite) and albite constitute the majority of the peaks present.

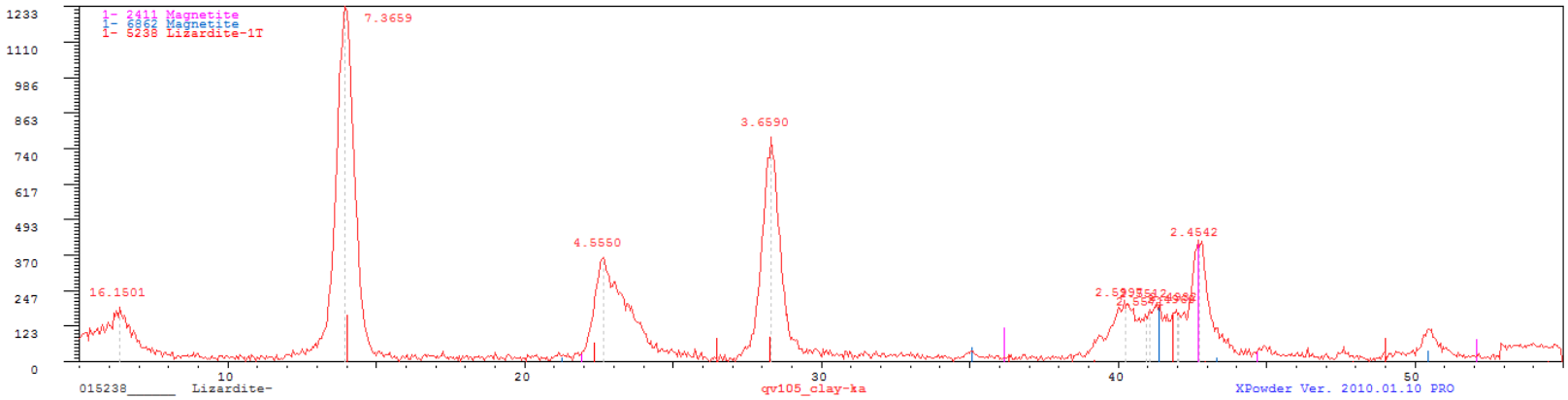

Fig. 20. Diffractogram from CROMO2-105 at 60 m depth shows a clay matrix in which the greenstone fragment (Fig. 20) is situated. The clay shows no sign of greenstone minerals and is composed almost entirely of lizardite and magnetite.

Fig. 21. Black, grey, and white clasts of serpentinite embedded in clay from CROMO2-121 at a depth of 21 m. Photo credit: A. McCann.

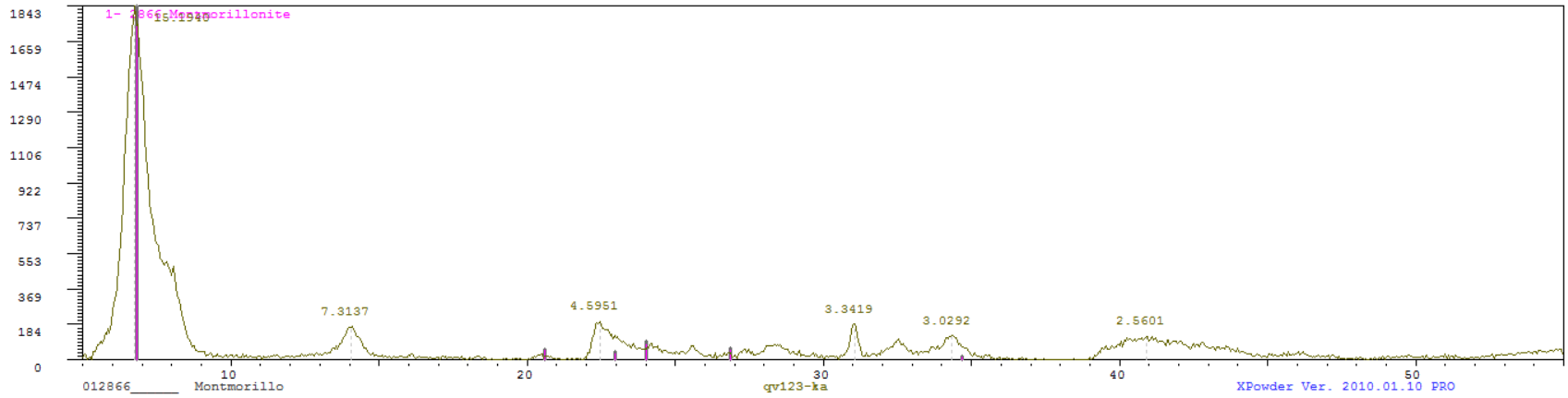

Fig. 22. Diffractogram from CROMO2-123 at 24.38 m depth. The small peak at 7.3 Å and 4.6 Å refer to lizardite, but the horizon is completely dominated by the presence of the clay, which is the tallest peak on the far left.

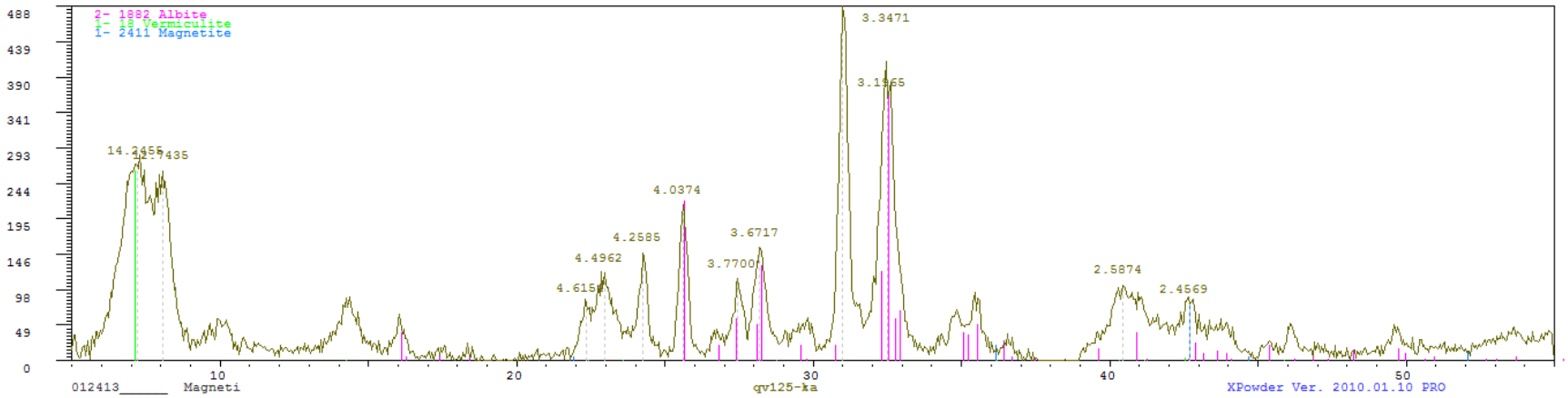

Fig. 23. Diffractogram from CROMO2-125 at 27.43 m depth depicts greenstone minerals albite (3.19 Å) and quartz (3.3 Å) as the dominant mineral phase along with clay minerals (14.2, 12.7 Å) and minor magnetite (2.5 Å). The highest peak between 4.6 Å and 12.7 Å may represent lizardite, as magnetite does not typically occur without accompanying lizardite in these cores.

Fig. 24. Greenstone and serpentine minerals lie in a muddy serpentine-rich clay matrix in a core from CROMO2-131 at 36 m depth. Photo credit: A. McCann.

Fig. 25. Serpentinite mass displaying schistose texture, visible by the friable black, white and light green massive minerals, in a core from CROMO2-131 at 36 m depth. Photo credit: A. McCann.

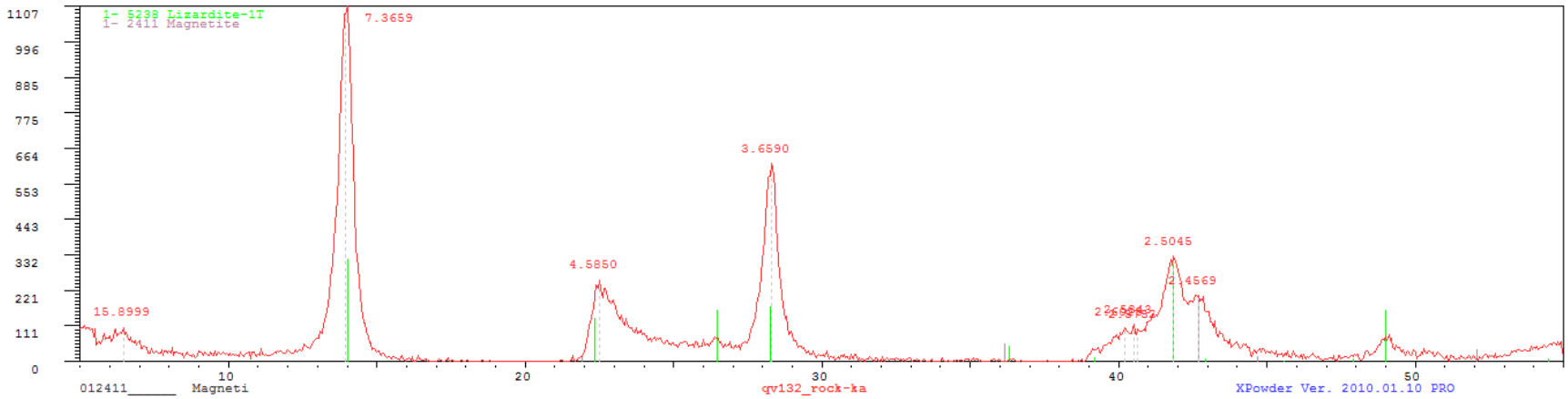

Fig. 26. Diffraction from CROMO2-132 at 37 m depth. The two highest peaks, at 7.3659 Å and 3.6590 Å correspond to lizardite peaks, and the group of peaks at 2.5045 Å and 2.4569 Å correspond to magnetite peaks. Clay peaks are rare in this sample, and would typically show up around the 15.9 Å.

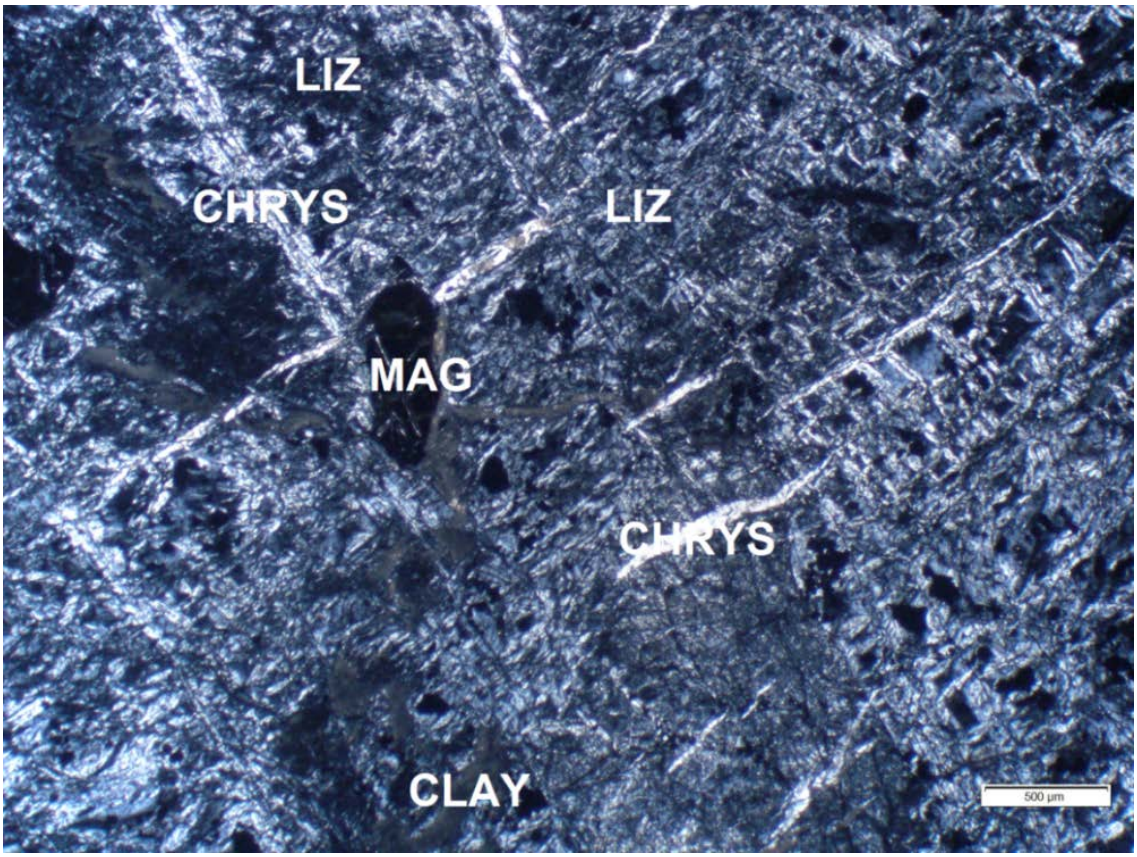

Fig. 27. 2x thin section from CROMO2-134 at 41.15 m depth. The thin section confirms the results from the XRD. Lizardite, the mesh-like white and blue matrix, makes up most of the slide, with white veinlets of chrysotile and scattered black blebs of magnetite. Some unidentifiable clay minerals are present as well as opaque brown steaks and smears.

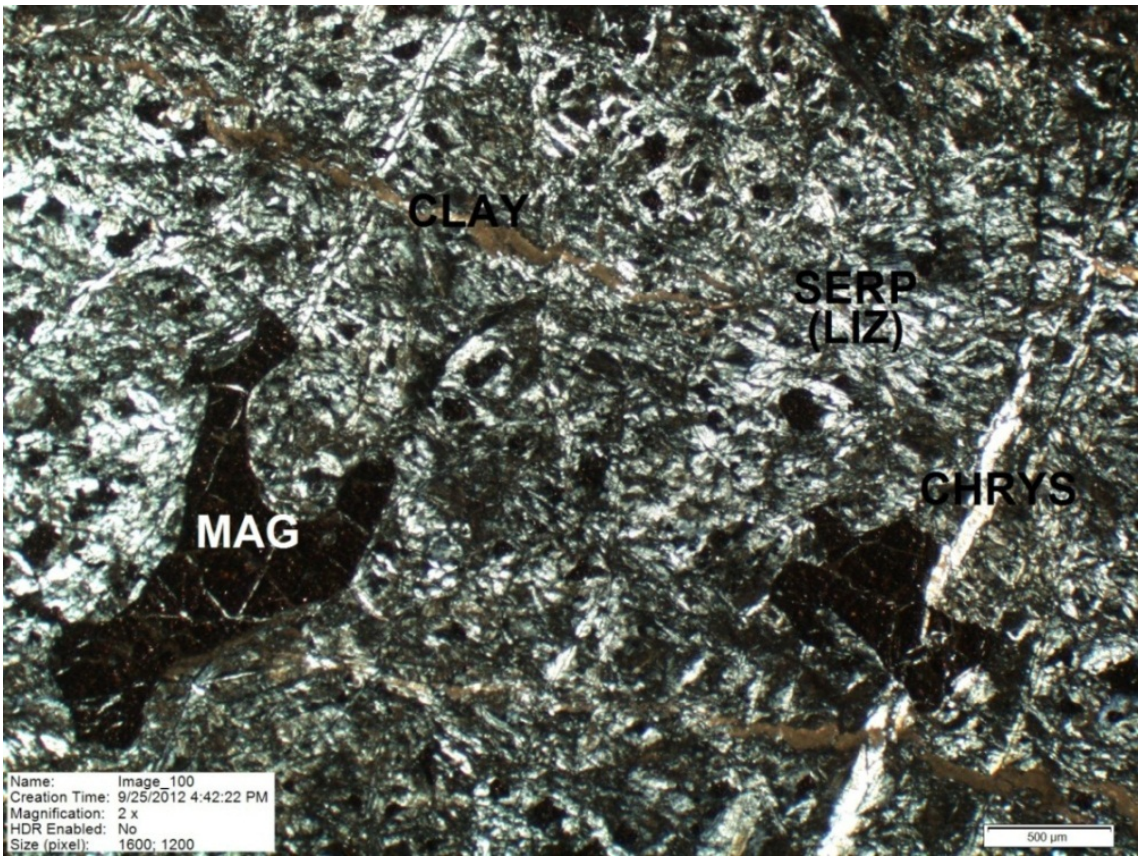

Fig. 28. Thin section from CROMO2-136 at 45.72 m depth. Thin section image confirms XRD data. The majority of the slide is lizardite, with veinlets of clay and chrysotile as well as angular crystals of magnetite.

Fig. 29. Hard cobbles of greasy serpentinite from CROMO2-136 at 44 m depth. Photo credit: A. McCann.

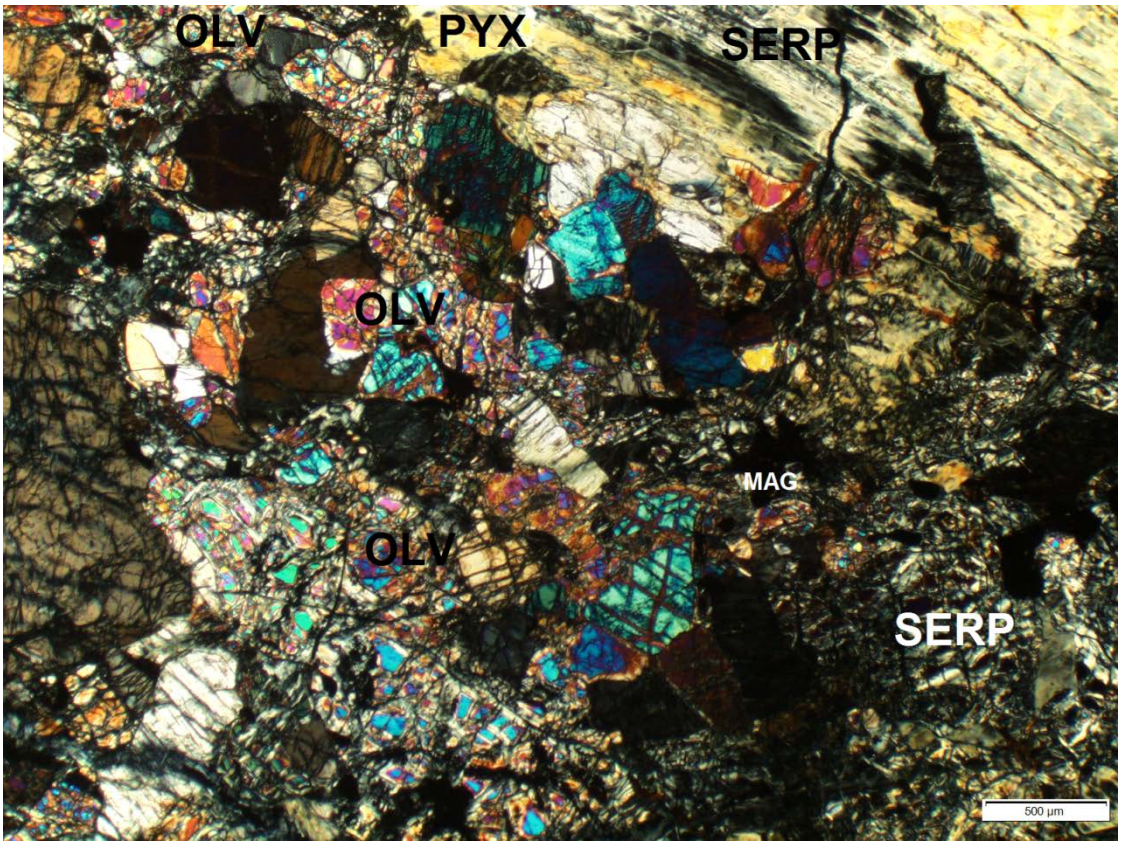

Fig. 30. Core sample from Homestake Mine Pit Borehole at 110 m depth. Sample shows 4 different mineral phases. Olivine is a low order birefringent mineral (i.e., under cross polarized light, olivine appears iridescent with bright, bold colors ranging across the spectrum

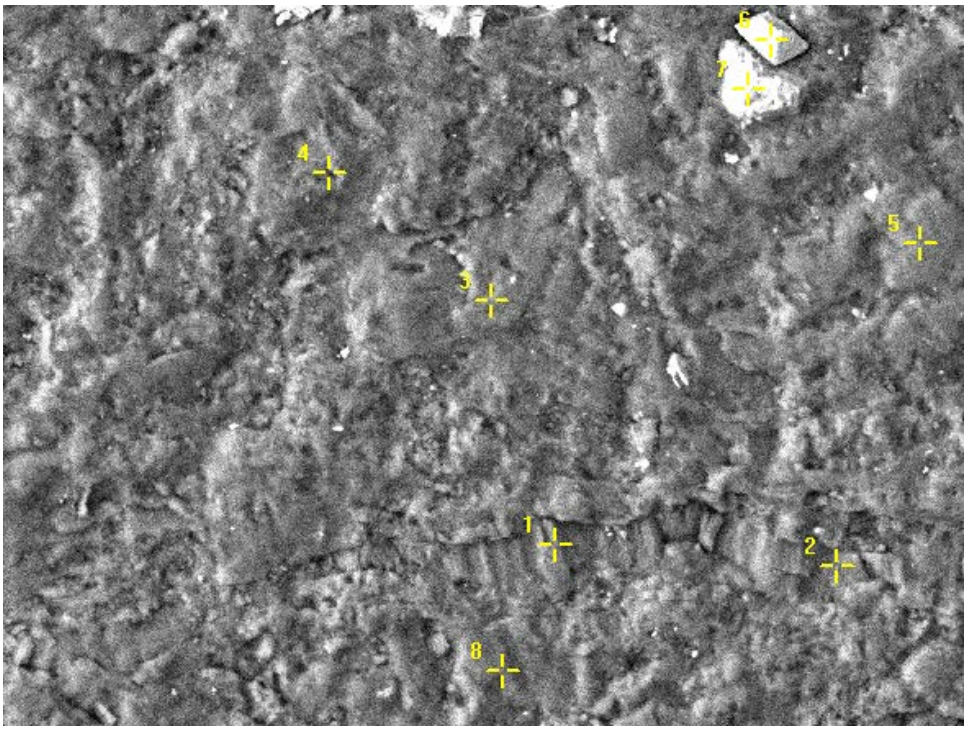

Fig. 31. 600X SEM backscatter image of a slide from CROMO2-134 at 40 m depth. Heavier elements show up as lighter shades on the image. The grey massive mineral in the image is lizardite (tags 3, 4, 5, and 8), and the white octahedral crystal (tag 6) is magnetite. Chrysotile is proposed as the mineral filling the fracture holding tags 1 and 2.

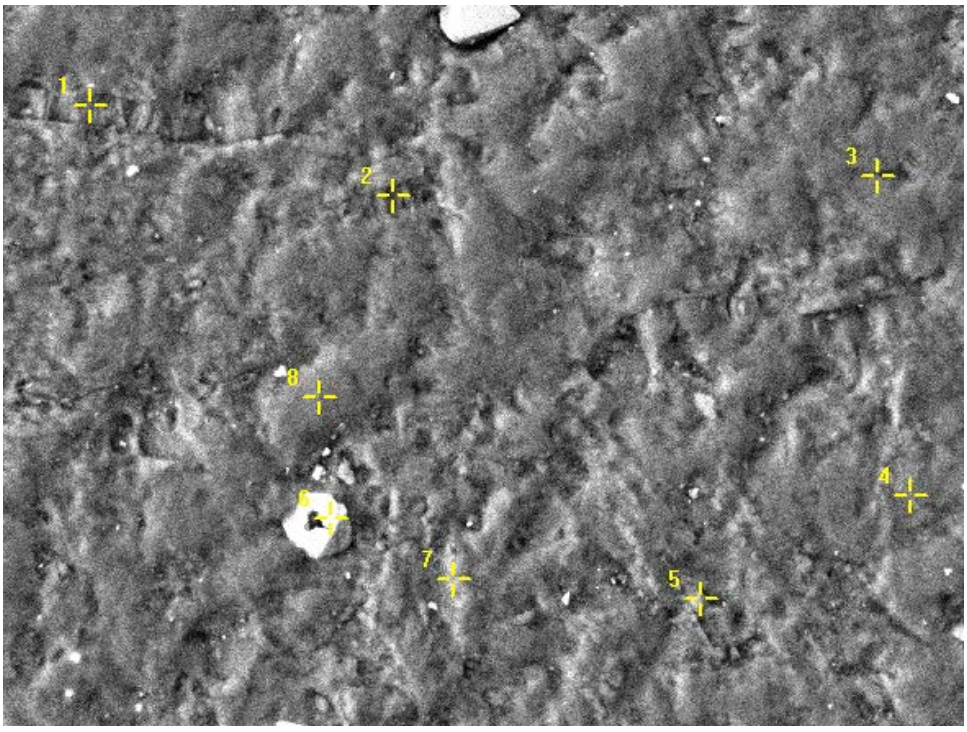

Fig. 32. 600X SEM backscatter image of a slide from CROMO2-134 at 40 m depth, at a different portion of the slide from the one in Fig. 31. Heavier elements show up as lighter colored on the image. The grey mineral in the image is lizardite and the two white minerals are crystals of magnetite.

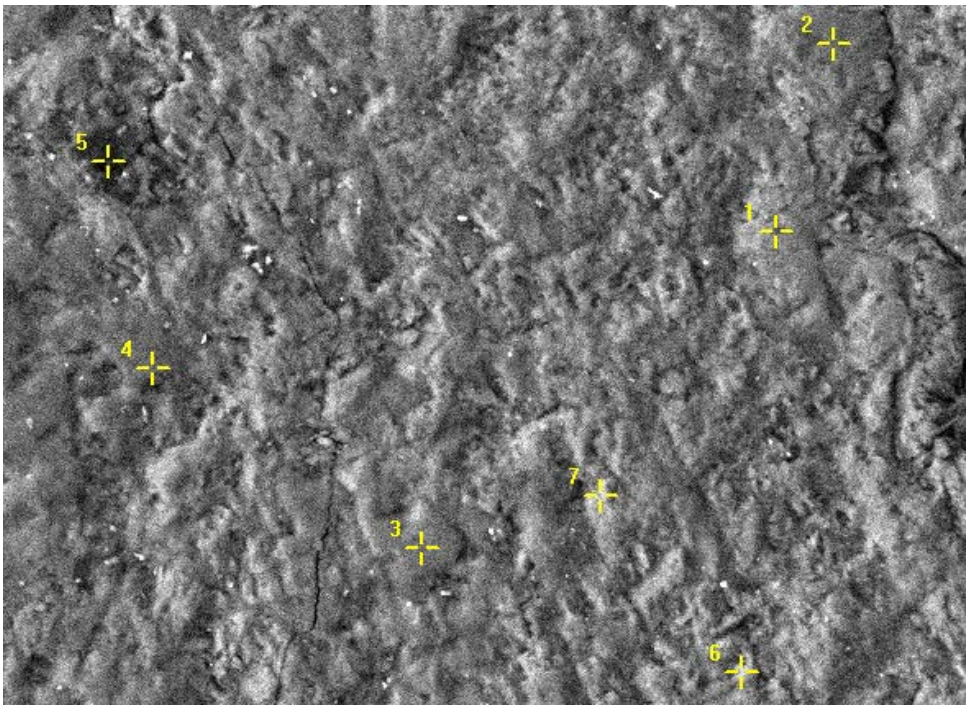

Fig. 33. 600X SEM backscatter image of a slide from CROMO2-136 at 43 m depth. Heavier elements show up as lighter shades on the image. The grey mineral in the image is lizardite and the white is magnetite.

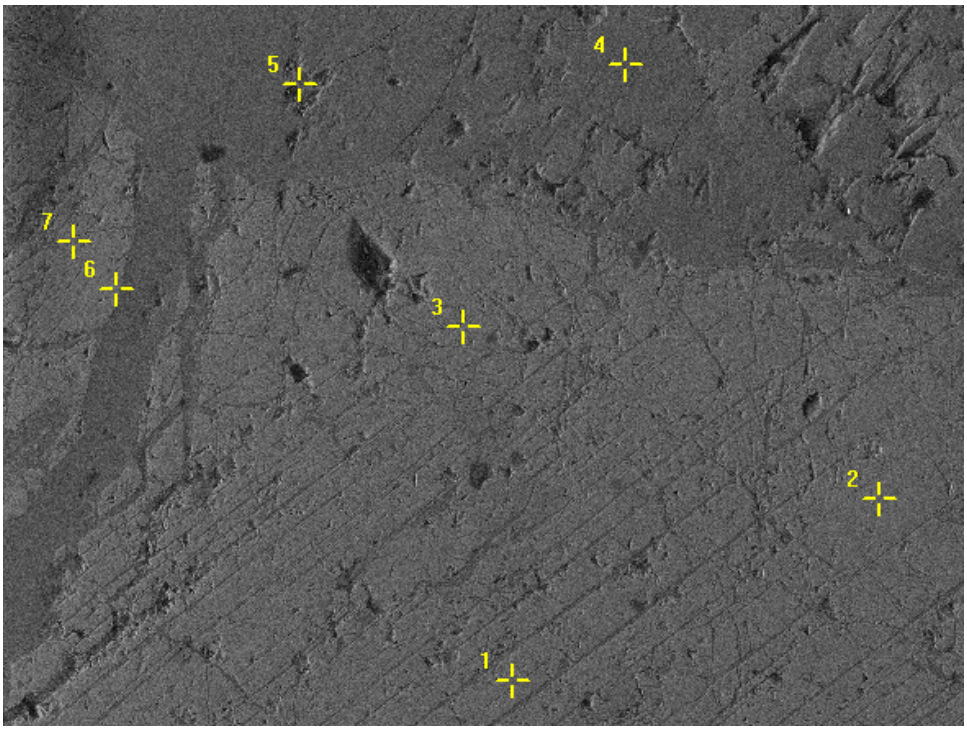

Fig. 34. 600X SEM backscatter image of a slide from Homestake Mine Pit Borehole (HMPB) core at 110 m depth. Heavier elements show up as lighter shades on the image. The darker grey mineral (tags 4 and 5) in the image is lizardite and the lighter grey mineral with the parallel cleavage plains is pyroxene (tags 1, 2, and 3).

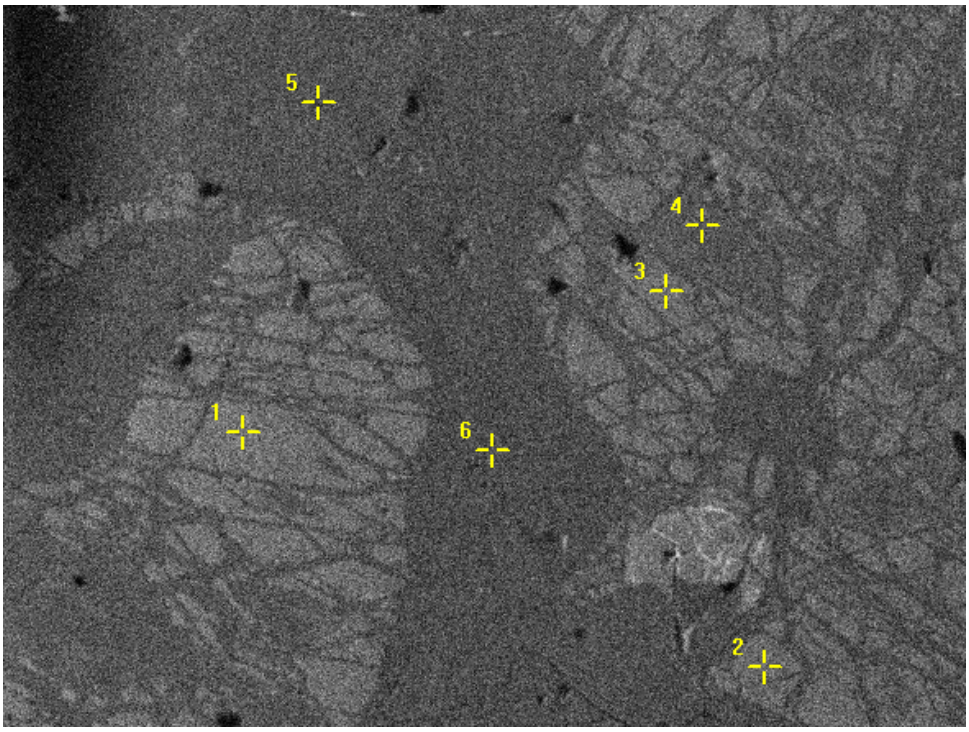

Fig. 35. 600X SEM backscatter image of a slide from HMPB core at 110 m depth. Heavier elements show up as lighter shades on the image. The darker grey mineral in the image is lizardite and the lighter grey mineral where tags 1, 2 and 3 are is pyroxene. The white streaks were not analyzed, but are almost certainly magnetite.

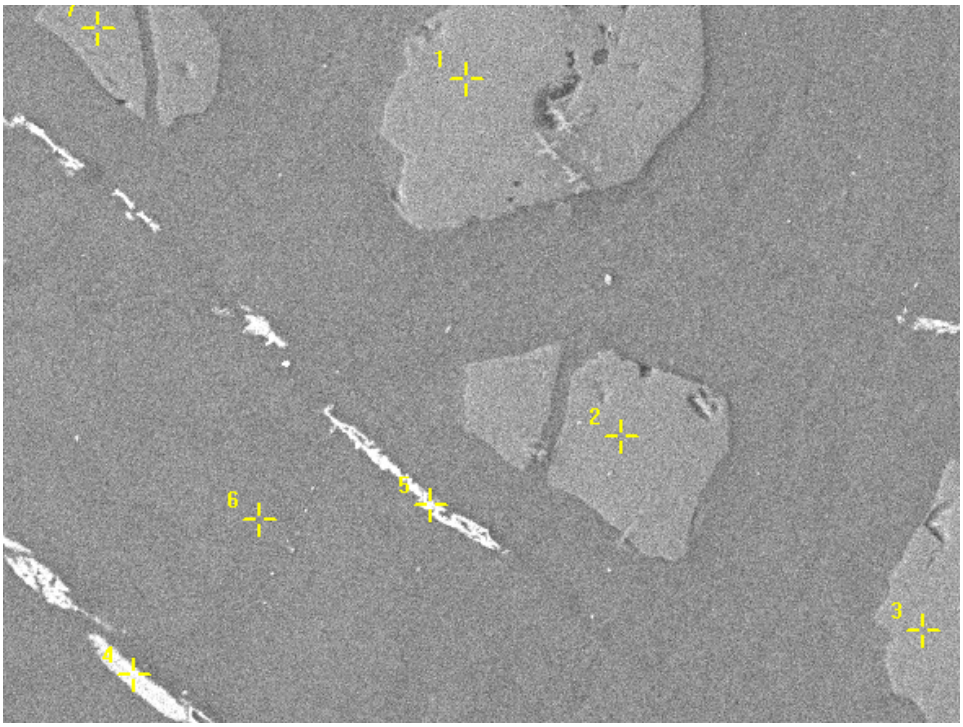

Fig. 36. 600X SEM backscatter image of a slide from HMPB core at 110 m depth. Heavier elements show up as lighter shades on the image. The darker grey mineral in the image is lizardite and the lighter grey mineral where tags 2 and 3 are is olivine. The white streaks are magnetite.

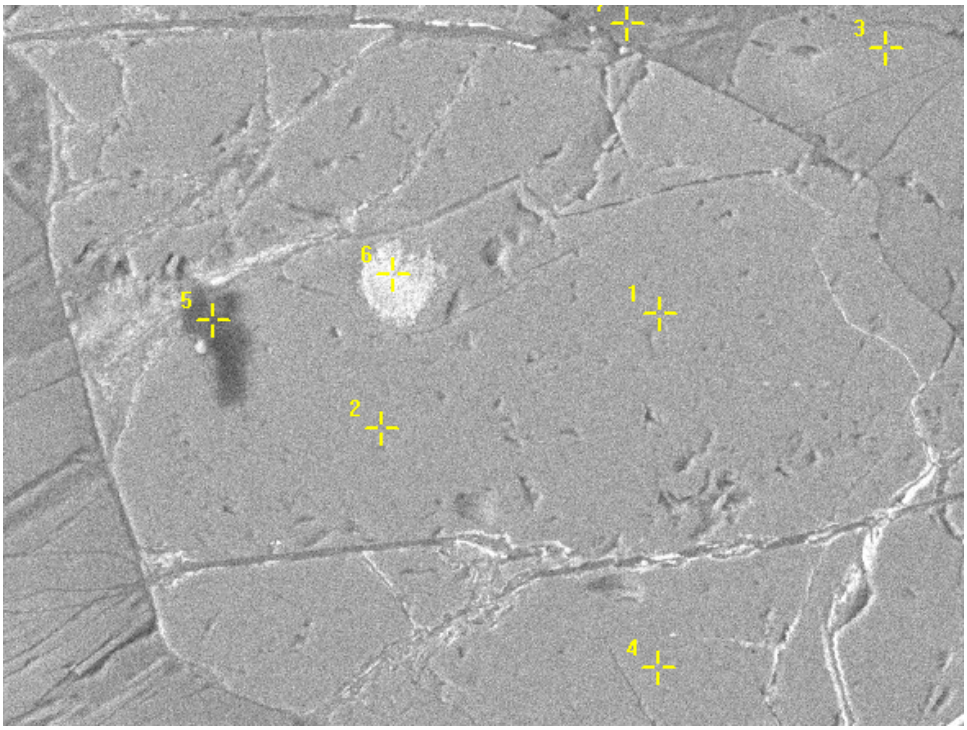

Fig. 37. 600X SEM backscatter image of a slide from HMPB core at 110 m depth. Heavier elements show up as lighter shades on the image. The large grain in the center of the screen is a magnesium-rich silica-poor aluminum oxide mineral. The elemental abundances are similar to that of a spinel group mineral, and spinel fits in with the petrology of the other rocks. The grain in the top right of the image, where tag 3 lies, is olivine. The white spot on tag 6 is magnetite.

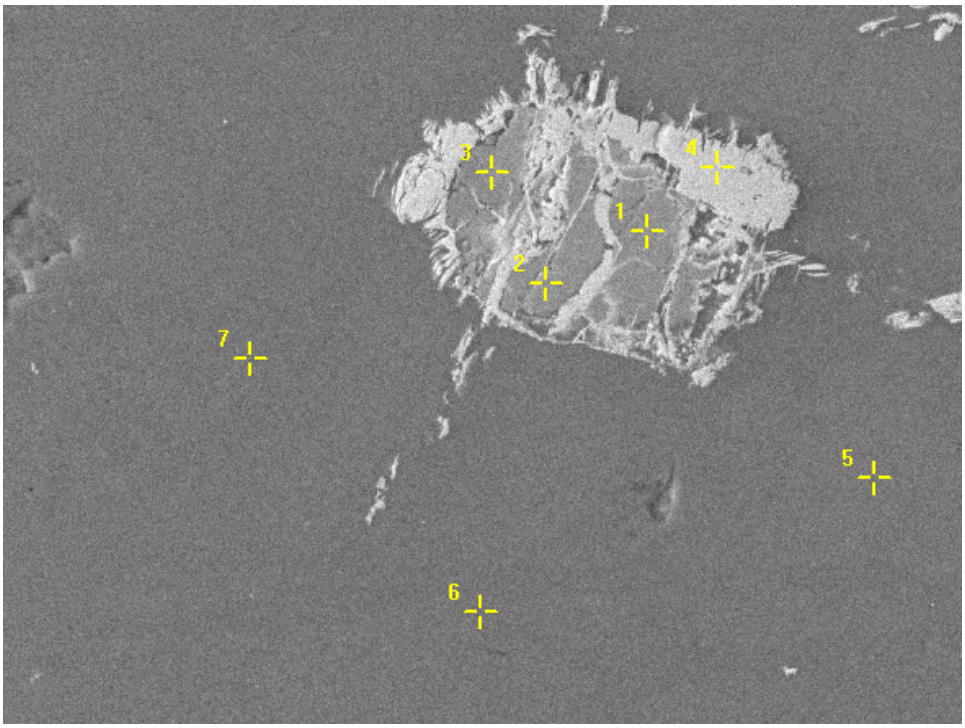

Fig. 38. 600X SEM backscatter image of a slide from HMPB core at 110 m depth. Heavier elements show up as lighter colored on the image. The grain in the center of the screen is a spinel, while the matrix is serpentine and the lightly colored veined mineral is magnetite.

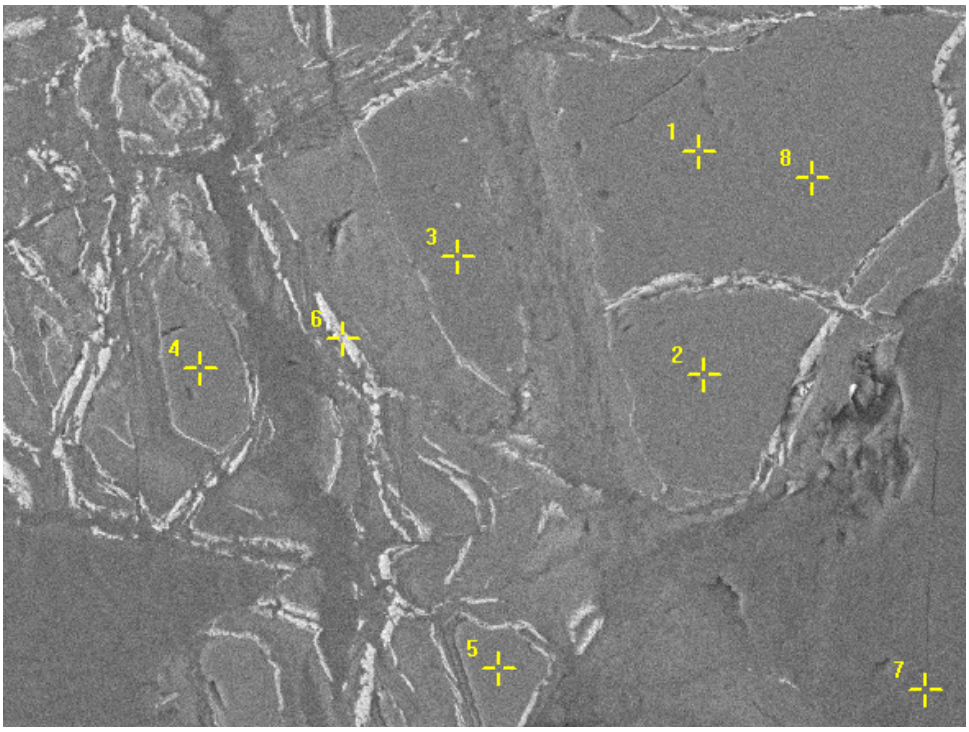

Fig. 39. 600X SEM backscatter image of a slide from HMPB core at 110 m depth. Heavier elements show up as lighter colored on the image. The fractured crystal with slightly higher relief than the groundmass is a spinel, while the groundmass itself is serpentine and the lightly colored veined mineral is magnetite.

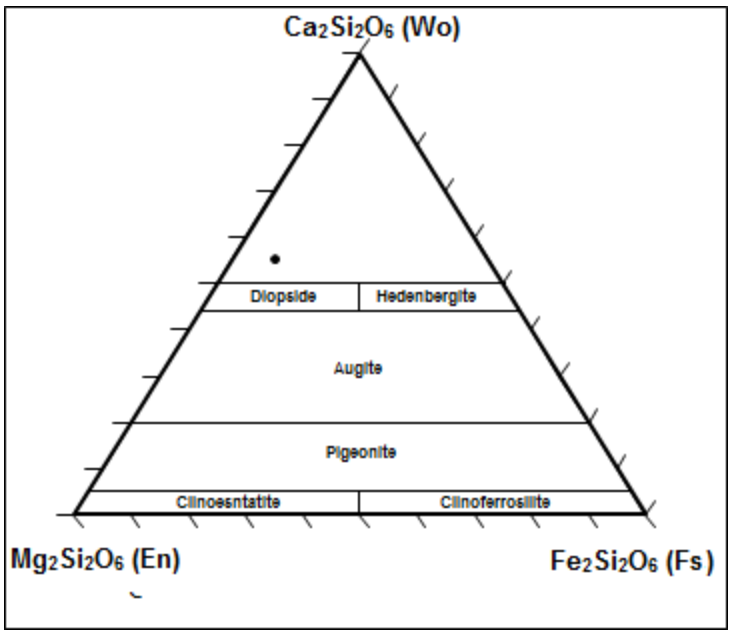

Fig. 40. Ternary displaying plot location of pyroxene found in CRO rocks. Fs = ferrosilite, En = enstatite, Wo = wollastonite. Created with TriPlot v. 1.4.2.

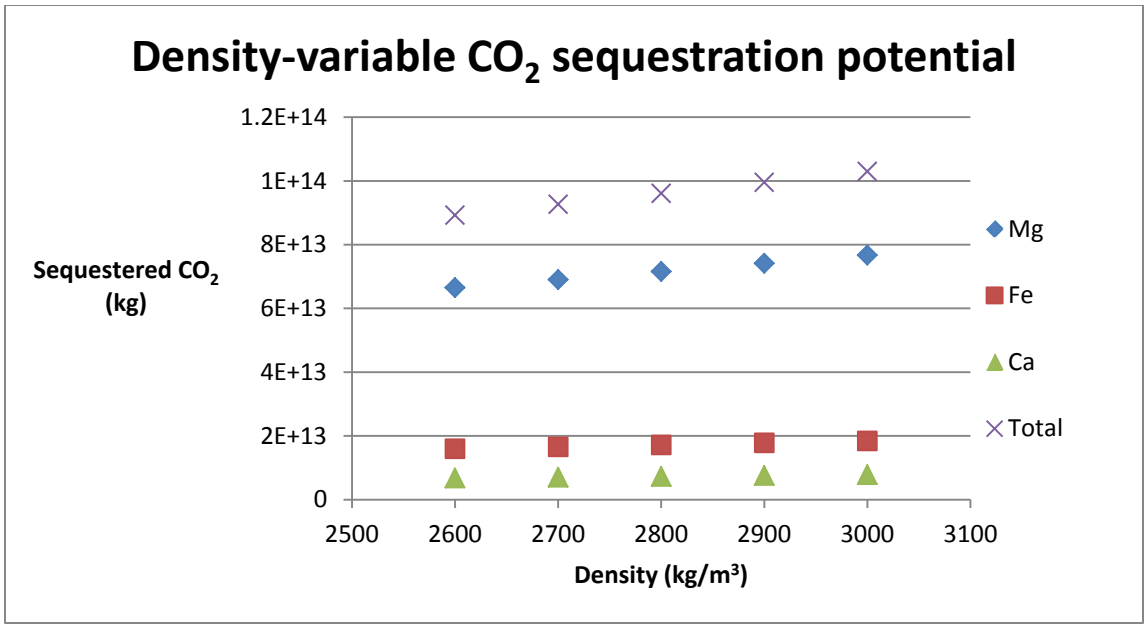

Fig. 41. Graph displaying maximum potential CO_2 sequestration potential with variable density, at 5 km depth, with olivine fraction fixed at 0.2.

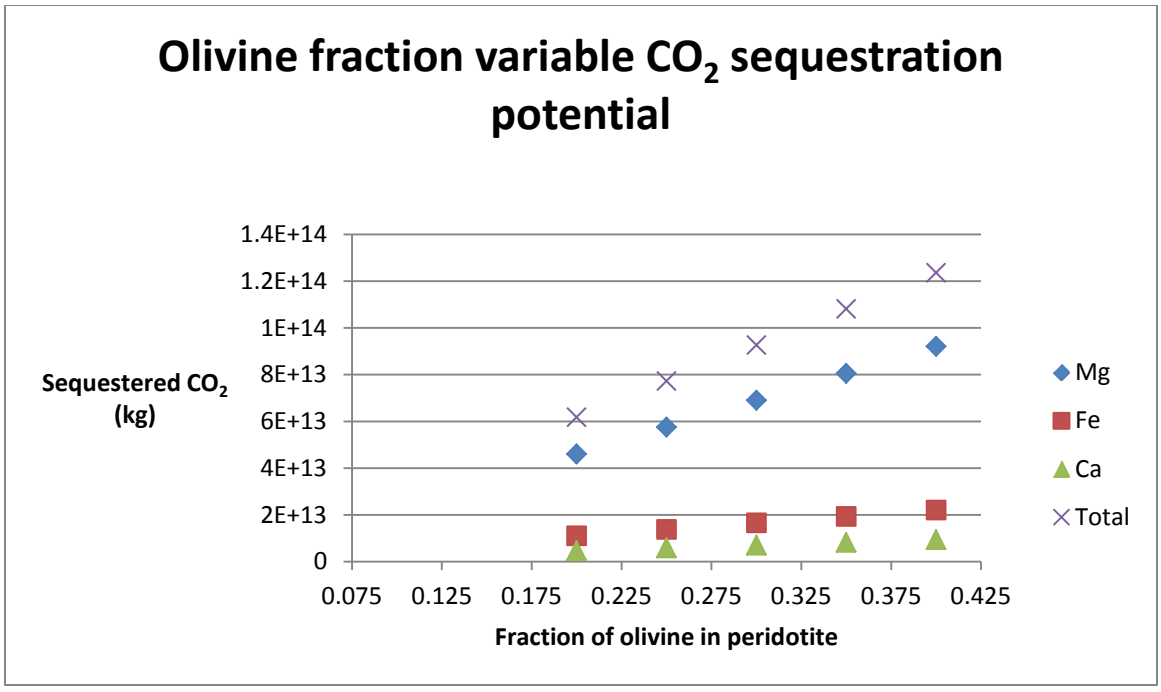

Fig. 42. Graph displaying maximum potential CO_2 sequestration potential at 5km depth, with density set at 2700 kg/m^3; these trends show how variable serpentinization in mantle rocks shifts the total possible mineralized CO_2 load

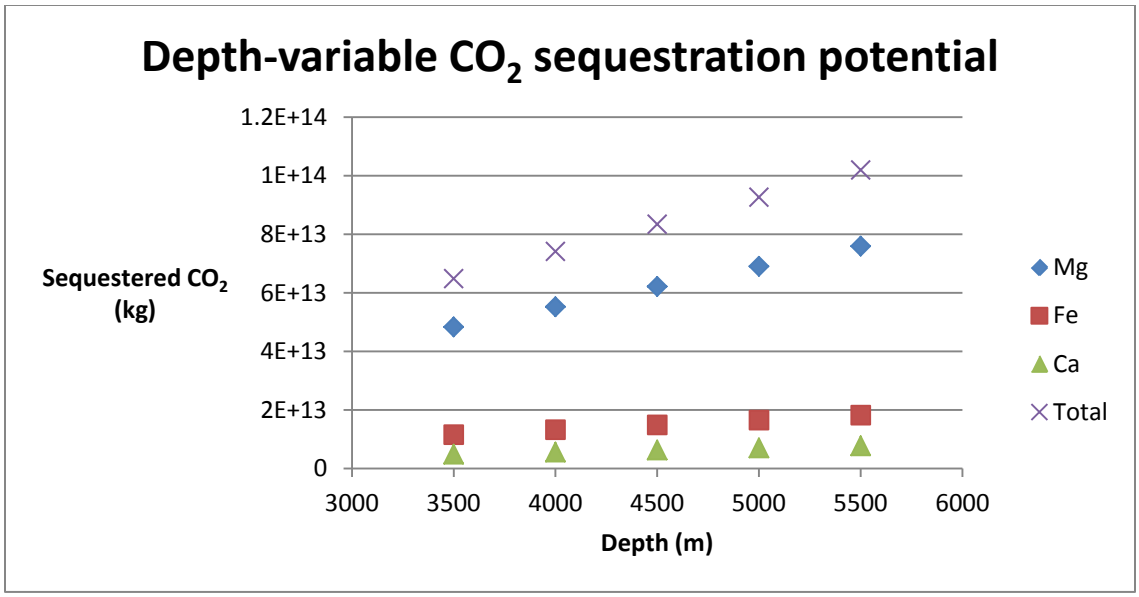

Fig. 43. Graph displaying maximum potential CO_2 sequestration potential for the CRO, given assumed basal depth of the ultramafic unit ranging from 3 to 6 km, with olivine fraction fixed at 0.2 and density set at 2700 kg/m^3.

Table 1

Table showing mineral presence in core samples CROMO1 (Core Shed Well) and CROMO2 (Quarry Valley) as determined by XRD.

Liz = lizardite, mag = magnetite, chlor = chlorite, trem = tremolite

Core	Depth (m)	Liz	Clay	Mag	Albite	Quartz	Chlor	Trem	Calcite
CROMO1 1	0.45		X	X	X	X			
CROMO1 2	0.91		X	X	X	X			
CROMO1 3	1.52		X	X	X	X			
CROMO1 4	1.98		X	X	X	X			
CROMO1 5	2.44	X	X	X	X	X			
CROMO1 6	3.05	X	X	X	X	X			
CROMO1 7	3.51	X	X	X	X	X			
CROMO1 8	3.96	X	X	X	X	X			
CROMO1 9	4.57	X	X	X	X	X			
CROMO1 10	8.15	NA	NA	NA	NA	NA	NA	NA	
CROMO1 11	8.61	X	X	X	X			X	
CROMO1 12	9.02	X	X	X				X	X
CROMO1 13	10.74	X	X	X				X	
CROMO1 14	12.65	X	X	X				X	
CROMO1 15	13.82	X		X					
CROMO1 16	16.76	X	X	X					
CROMO1 17	18.29	X	X	X					
CROMO1 18	19.81	X	X	X					
CROMO1 19	21.34	X		X					
CROMO1 20	22.86	NA	NA	NA	NA	NA	NA	NA	
CROMO1 21	22.86	X		X					
CROMO1 22	24.38	X		X					
CROMO1 23	25.91	X		X					
CROMO1 24	27.43	X		X					
CROMO1 25	27.97	X	X	X	X		X	X	X
CROMO1 26	28.50	X			X		X	X	
CROMO1 27	28.96	X			X		X	X	
CROMO1 28	30.48						X		
CROMO1 29	31.09				X			X	
CROMO2 100	0.46	X		X					
CROMO2 102	1.37	X		X					
CROMO2 103	5.03								
CROMO2 104	5.49	X		X					

CROMO2 105	6.10	X		X	X		X		
CROMO2 106	6.55	X		X					
CROMO2 107	7.01	X		X					
CROMO2 108	7.62	X		X					
CROMO2 109	8.08	X		X					
CROMO2 110	8.53	X		X					
CROMO2 111	9.14	X		X					
CROMO2 112	9.60	X		X					
CROMO2 113	10.06	X		X					
CROMO2 114	10.67	X		X					
CROMO2 115	10.92	X							
CROMO2 116	14.78	N/A	N/A	N/A	N/A	N/A			
CROMO2 117	15.24	X		X					
CROMO2 118	16.76	X		X					
CROMO2 119	18.29	X		X					
CROMO2 120	19.81		X						
CROMO2 121	21.34	X	X	X	X	X			
CROMO2 122	22.86	X		X					
CROMO2 123	24.38		X						
CROMO2 124	25.91		X						
CROMO2 125	27.43	X	X	X	X				
CROMO2 126	28.96	X	X	X	X	X			
CROMO2 127	30.48		X	X	X				
CROMO2 128	32.00	X	X	X	X	X			
CROMO2 129	33.53	X	X	X	X	X			
CROMO2 130	35.05				X	X	X		
CROMO2 131	36.58	X	X	X					
CROMO2 132	38.10	X		X					
CROMO2 133	39.62	X		X					
CROMO2 134	41.15	X		X					
CROMO2 135	42.67	X		X					
CROMO2 136	44.20	X		X					
CROMO2 137	45.72	X		X					

Table 2

Typical element concentrations in common and uncommon (wollastonite) ultramafic minerals encountered in ophiolitic rocks, based solely on chemical formula. Olivine and wollastonite have the highest percentage of divalent cations among the listed minerals, where talc and serpentine have the lowest percentages.

Mineral	%Mg	%Fe	%Si	%H	%O	%Ca
Serpentine (including lizardite, antigorite, chrysotile, based on $(Mg_{2.25}Fe^{2+}_{0.75}Si_2O_5(OH)_4)$	18.18	13.93	18.68	1.34	47.88	0
Olivine (based on $Mg_{1.6}Fe_{0.4}SiO_4$)	25.37	14.57	18.32	0	41.74	0
Talc (based on $Mg_3Si_4O_{10}(OH)_2$)	19.23	0.53	29.62	0	50.62	0
Diopside (pyroxene) (based on $CaMgSi_2O_6$)	11.22	0	25.94	0	44.33	34.5
Wollastonite (based on $CaSiO_3$)	0	0	24.18	0	41.32	34.5

Table 3

CROMO2-134 oxide wt% and wt% of the serpentine phases from Fig. 31 at 40 m depth, as determined by SEM-EDS.

Slide	Tag		Mg	Fe	Si	Ca	Al
IYO9-1	1		37.52	11.22	48.76	1.04	0.40
IYO9-1	2		37.12	12.61	49.13	0.51	0.23
IYO9-1	5		37.64	13.77	47.30	0.49	0.15
IYO9-1	8		35.42	15.72	46.98	0.61	0.18
		oxide					
Average		wt%	36.93	13.33	48.04	0.66	0.24
		c.f.	0.603	0.7773	0.46	0.717	0.5293
Average		wt%	22.27	10.36	22.10	0.48	0.13

Table 4

CROMO2-134 oxide wt % and wt% of the magnetite phases from the magnetite in Fig. 31 from 40 m depth, as determined by SEM-EDS. Magnetite (Fe_3O_4) is the most iron-rich mineral phase found in CRO rocks and appears in every thin section. Formation and occurrence of magnetite are discussed in further detail in section 4.2.1.

Thin Section	Tag		Mg	Fe	Si	Ca	Al
IYO9-Magnetite	6		4.72	90.52	3.71	0.35	0.32
Average		oxide wt%	4.72	90.52	3.71	0.35	0.32
		c.f.	0.603	0.7773	0.46	0.717	0.5293
Average		wt%	2.85	70.36	1.71	0.25	0.17

Table 5

CROMO2-134 thin section wt% of the serpentine phases from Fig. 32 at 40 m depth, as determined by SEM-EDS.

Slide	Tag		Mg	Fe	Si	Ca	Al
IYO9-Serp	1		34.7	17.32	47.73	0	0
IYO9-Serp	2		32.56	22.36	42.88	0.8	0.22
IYO9-Serp	3		35.42	15.11	46.84	0.11	0
IYO9-Serp	4		36.79	14.44	47.47	0.86	0
IYO9-Serp	5		36.94	14.58	46.32	0.49	0.29
IYO9-Serp	7		38.99	11.37	48.54	0.45	0.16
		oxide					
Average		wt%	35.9	15.86	46.63	0.45	0.11
		c.f.	0.603	0.7773	0.46	0.717	0.5293
Average		wt%	21.65	12.33	21.45	0.32	0.059

Table 6

CROMO2-136 wt% of elements of the serpentine phases from the image in Fig. 32 at 40 m depth, as determined by SEM-EDS.

Slide	Tag		Mg	Fe	Si	Ca	Al
IYO10-Serp	1		35.53	16.18	46.67	0.22	0.12
IYO10-Serp	2		37.85	11.39	49.42	0	0.10
IYO10-Serp	3		37.45	14.77	46.31	0.56	0
IYO10-Serp	4		36.53	11.06	50.92	0.71	0
IYO10-Serp	6		38.14	15.51	44.48	0	0
IYO10-Serp	7		37	15.15	47.13	0.15	0
		oxide					
Average		wt%	37.08	14.01	47.49	0.27	0.037
		c.f.	0.603	0.777	0.46	0.717	0.529
Average		wt%	22.36	10.89	21.85	0.20	0.019

Table 7

Serpentine phase mineral weight percentages from HMPB slide (Fig. 34) at 110 m depth, as determined by SEM-EDS.

Slide	Tag		Mg	Fe	Si	Ca	Al
HMPB_Deep_Serp	4		30.77	15.51	43.60	1.93	6.51
HMPB_Deep_Serp	5		30.32	16.39	47.56	1.79	2.49
		oxide					
Average		wt%	30.55	15.95	45.58	1.86	4.5
		c.f.	0.603	0.7773	0.46	0.717	0.5293
Average		wt%	18.42	12.40	20.97	1.33	2.38

Table 8

Pyroxene phase mineral weight percentages from HMPB slide (Fig. 34) at 110 m depth, as determined by SEM-EDS.

Slide	Tag		Mg	Fe	Si	Ca	Al
HMPB_Deep_Pyx	1		12.14	5.90	43.93	29.54	6.18
HMPB_Deep_Pyx	2		11.87	4.05	44.22	33.06	5.33
HMPB_Deep_Pyx	7		12.72	5.19	43.93	30.58	6.13
		oxide					
Average		wt%	12.24	5.05	44.03	31.06	5.88
		c.f.	0.603	0.7773	0.46	0.717	0.5293
Average		wt%	7.383	3.93	20.25	22.27	3.11

Table 9

Serpentine phase mineral weight percentages from HMPB slide (Fig. 35) at 110 m depth, as determined by SEM-EDS.

Slide	Tag		Mg	Fe	Si	Ca	Al
HMPB_Deep_Serp3	5		38.45	11.63	47.62	0.68	0.80
HMPB_Deep_Serp3	6		33.04	17.20	45.23	1.63	2.14
		oxide					
Average		wt%	35.75	14.42	46.43	1.16	1.47
		c.f.	0.603	0.7773	0.46	0.717	0.5293
Average		wt%	21.55	11.21	21.36	0.828	0.78

Table 10

Pyroxene phase mineral weight percentages from HMPB slide (Fig. 35) at 110 m depth, as determined by SEM-EDS.

Slide	Tag		Mg	Fe	Si	Ca	Al
HMPB_Deep_Pyx3	1		14.16	7.33	44.36	27.87	5.03
HMPB_Deep_Pyx3	2		14.36	4.35	45.16	29.14	5.23
HMPB_Deep_Pyx3	3		13.69	5.70	44.34	27.88	6.00
		oxide					
Average		wt%	14.07	5.79	44.62	28.30	5.42
		c.f.	0.603	0.7773	0.46	0.717	0.5293
Average		wt%	8.484	4.50	20.53	20.29	2.87

Table 11

Serpentine phase mineral weight percentages from HMPB slide (Fig. 36) at 110 m depth as determined by SEM-EDS.

Slide	Tag		Mg	Fe	Si	Ca	Al
HMPB_Deep_SERP	6		37.33	13.15	48.36	0.2	0.86
		oxide					
Average		wt%	37.33	13.15	48.36	0.2	0.86
		c.f.	0.603	0.7773	0.46	0.717	0.5293
Average		wt%	22.51	10.22	22.25	0.14	0.46

Table 12

Olivine phase mineral weight percentages from HMPB slide (Fig. 36) at 110 m depth, as determined by SEM-EDS.

Slide	Tag		Mg	Fe	Si	Ca	Al
HMPB_Deep_OLV1	1		39.69	18.61	41.62	0	0.09
HMPB_Deep_OLV1	2		39.73	19.75	39.64	0	0.31
HMPB_Deep_OLV1	3		41.27	17.12	40.63	0	0
HMPB_Deep_OLV1	7		41.77	13.66	44.15	0.27	0.16
		oxide					
Average		wt%	40.62	17.285	41.51	0.068	0.14
		c.f.	0.603	0.7773	0.46	0.717	0.5293
Average		wt%	24.49	13.44	19.10	0.048	0.074

Table 13

Olivine phase mineral weight percentages from HMPB slide (Fig. 37) at 110 m depth, as determined by SEM-EDS.

Slide	Tag		Mg	Fe	Si	Ca	Al
HMPB_Deep_OLV4	3		28.90	13.40	50.67	0.69	4.84
		oxide					
Average		wt%	28.9	13.4	50.67	0.69	4.84
		c.f.	0.603	0.7773	0.46	0.717	0.5293
Average		wt%	17.43	10.42	23.31	0.49	2.56

Table 14

Spinel phase mineral weight percentages from HMPB slide (Fig. 37) at 110 m depth, as determined by SEM-EDS. Spinel holds much more chromium and aluminum than any other mineral in the CRO.

Thin Section	Tag		Mg	Fe	Si	Ca	Al	Cr
HMPB_Deep_Spn4	1		15.34	22.71	4.26	0	40.38	17.26
HMPB_Deep_Spn4	2		16.60	19.05	5.66	0	45.2	13.29
HMPB_Deep_Spn4	4		15.99	18.53	5.48	0.49	42.99	16.52
HMPB_Deep_Spn4	5		15.53	23.80	9.94	0.90	37.61	11.11
		oxide						
Average		wt%	15.87	21.02	6.34	0.35	41.55	14.55
		c.f.	0.603	0.7773	0.46	0.717	0.5293	0.6842
Average		wt%	9.567	16.34	2.91	0.25	21.99	9.952

Table 15

Spinel phase mineral weight percentages from HMPB slide (Fig. 38) at 110 m depth, as determined by SEM-EDS. The spinel holds much more chromium and aluminum than any other mineral in the CRO.

Thin Section	Tag		Mg	Fe	Si	Ca	Al	Cr
HMPB_Deep_Spn5	1		12.98	38.18	5.87	0	29.52	13.04
HMPB_Deep_Spn5	2		13.58	36.39	6.01	0	31.01	12.24
HMPB_Deep_Spn5	3		13.93	36.82	5.92	0	31.19	11.52
		oxide						
Average		wt%	13.50	37.13	5.93	0	30.57	12.27
		c.f.	0.603	0.7773	0.46	0.717	0.5293	0.6842
Average		wt%	8.139	28.86	2.73	0	16.18	8.393

Table 16

Serpentine phase mineral weight percentages from HMPB slide (Fig. 38) at 110 m depth, as determined by SEM-EDS.

Thin Section	Tag		Mg	Fe	Si	Ca	Al
HMPB_Deep_Serp5	5		35.82	14.90	48.04	0	0.43
HMPB_Deep_Serp5	6		34.58	14.67	49.94	0.18	0
HMPB_Deep_Serp5	7		36.81	13.57	48.92	0.35	0
		oxide					
Average		wt%	35.74	14.38	48.97	0.18	0.14
		c.f.	0.603	0.7773	0.46	0.717	0.5293
Average		wt%	21.55	11.18	22.53	0.13	0.076

Table 17

Serpentine phase mineral weight percentages from HMPB slide (Fig. 39) at 110 m depth, as determined by SEM-EDS.

Thin Section	Tag		Mg	Fe	Si	Ca	Al
HMPB_Deep_Serp6	7		32.8	19.81	41.21	0	4.58
		oxide					
Average		wt%	32.8	19.81	41.21	0	4.58
		c.f.	0.603	0.777	0.46	0.717	0.529
Average		wt%	19.78	15.40	18.96	0	2.42

Table 18

Spinel phase mineral weight percentages from HMPB slide (Fig. 39) at 110 m depth.

Thin Section	Tag		Mg	Fe	Si	Ca	Al	Cr
HMPB_Deep_Spn6	1		16.28	20.22	5.76	0.52	41.4	15.82
HMPB_Deep_Spn6	3		16.17	24.48	5.34	0.12	39.78	14.10
HMPB_Deep_Spn6	4		15.60	23.47	5.13	0.12	40.76	14.05
HMPB_Deep_Spn6	5		15.96	22.08	5.98	0	40.09	15.34
HMPB_Deep_Spn6	8		15.90	20.11	4.96	0	43.65	14.69
		oxide						
Average		wt%	15.98	22.07	5.434	0.15	41.14	14.80
		c.f.	0.603	0.7773	0.46	0.717	0.529	0.684
Average		wt%	9.637	17.16	2.50	0.11	21.77	10.12

Table 19

Combined averages for the elemental weight percentages of each of the major mineral phases in the core samples from CROMO1, CROMO2, and HMPB.

Serpentine

Element	Mg	Fe	Si	Ca	Al
Wt%	21.49	11.49	21.66	0.33	0.42

Olivine

Element	Mg	Fe	Si	Ca	Al
Wt%	24.37	13.44	19.10	0.041	0.074

Pyroxene

Element	Mg	Fe	Si	Ca	Al
Wt%	7.89	4.21	20.39	21.21	3.00

Spinel

Element	Mg	Fe	Si	Ca	Al	Cr
Wt%	7.92	29.89	2.67	0.11	15.99	8.03

Table 20
Bulk solid XRF data for CROMO1 cores. Units for all values in ppm.

Segment	Depth (m)	Zr	Sr	Rb	Pb	As	Zn	Ni	Co	Ca	Fe	Mn	Cr	V	Ti	K
CROMO1 1	0.45	0	75	17	0	0	29	85	0	43066	121120	2119	56	295	2598	6876
CROMO1 2	0.91	150	174	43	12	0	79	258	0	8962	62850	2149	409	135	3552	9359
CROMO1 3	1.52	132	156	34	15	13	73	254	0	9183	68577	1308	320	216	3403	7585
CROMO1 4	1.98	76	101	20	0	0	37	119	0	7524	25112	295	236	175	3352	7383
CROMO1 5	2.44	104	105	26	0	0	49	128	0	5166	33183	322	149	104	2207	4834
CROMO1 6	3.05	145	116	25	0	8	41	671	0	9287	54323	1038	1176	147	3465	7477
CROMO1 7	3.51	43	170	31	11	8	37	1730	368	8588	56739	838	693	103	1832	6616
CROMO1 8	3.96	31	64	10	0	0	23	1692	0	8982	64099	2747	1758	139	1641	2793
CROMO1 9	4.57	168	538	18	0	9	51	413	0	42418	66822	1177	1280	206	3779	5128
CROMO1 10	8.15	44	113	0	0	0	22	1233	0	18168	84036	1154	1474	130	3743	498
CROMO1 11	8.61	10	123	0	0	26	0	1789	292	18384	65185	956	2060	104	955	0
CROMO1 12	9.02	18	184	0	8	0	0	1652	253	17279	74545	2148	1221	121	2148	2118
CROMO1 13	10.74	79	67	0	0	0	66	616	0	39704	68759	2245	420	166	3199	308
CROMO1 14	12.65	32	114	0	0	8	32	1550	0	36938	65054	1204	1935	141	2280	371
CROMO1 15	13.82	0	41	0	0	0	0	1705	0	4860	48629	773	1884	54	299	0
CROMO1 16	16.76	0	93	0	0	0	0	1705	270	8599	52580	911	1351	65	337	0
CROMO1 17	18.29	0	113	0	0	0	0	1385	0	4483	75711	990	1541	141	877	0
CROMO1 18	19.81	0	124	0	0	14	0	3754	371	8277	53873	866	1827	85	752	0
CROMO1 19	21.34	0	55	0	0	0	0	2147	0	2567	61354	925	2533	0	148	264
CROMO1 21	22.86	7	74	0	0	0	0	1467	302	17973	50545	986	1949	120	1277	524
CROMO1 22	24.38	0	38	0	0	0	0	1624	220	1574	42905	731	1120	0	114	253
CROMO1 23	25.91	0	52	0	0	0	0	1966	292	2440	49707	703	1779	0	202	0

Segment	Depth (m)	Zr	Sr	Rb	Pb	As	Zn	Ni	Co	Ca	Fe	Mn	Cr	V	Ti	K
CROMO1 24	27.43	71	170	5	0	0	39	106	0	29645	70258	1815	244	208	4700	1906
CROMO1 25	27.97	54	538	0	13	0	28	0	0	74291	69891	1409	0	253	3780	0
CROMO1 27	28.96	22	334	0	0	0	50	576	0	67044	56193	1432	860	183	2289	1157
CROMO1 28	30.48	13	194	0	0	0	0	0	0	46488	47998	1109	0	194	1799	1139

Table 21

Bulk solid XRF data for CROMO2 cores. Units for all values in ppm.

Segment	Depth (m)	Zr	Sr	Rb	Pb	Zn	Ni	Co	Ca	Fe	Mn	Cr	V	Ti	K
CROMO2 100	0.46	9	49	0	0	0	2151	284	9016	45995	742	835	58	399	1025
CROMO2 101	0.91	0	0	0	0	0	2191	237	313	40844	551	592	31	0	0
CROMO2 102	1.37	0	6	0	0	0	2581	426	780	52611	690	1497	62	0	213
CROMO2 103	6.55	0	13	0	0	0	2113	330	0	54303	709	771	0	0	0
CROMO2 104	7.01	0	33	0	0	0	1637	0	2513	48491	841	956	0	402	0
CROMO2 105	6.10	0	13	0	0	0	2445	247	0	56531	624	1460	54	0	0
CROMO2 106	6.55	0	21	0	0	0	1757	222	2295	43454	598	706	46	220	0
CROMO2 107	7.01	0	11	0	0	0	1999	0	0	47846	584	895	0	0	210
CROMO2 108	7.62	0	9	0	0	25	1641	167	0	40759	708	1074	50	0	0
CROMO2 109	8.08	0	14	0	0	0	2407	225	322	50937	623	1148	44	0	0
CROMO2 110	8.53	0	13	0	0	21	2018	0	298	46077	637	1247	0	0	0
CROMO2 111	9.14	0	7	0	0	0	2457	347	0	63440	568	856	0	0	253
CROMO2 112	9.60	0	12	0	0	0	1973	241	416	42794	523	1303	0	0	0
CROMO2 113	10.06	0	9	0	0	0	2860	185	280	51565	707	1874	43	0	0
CROMO2 114	10.67	0	11	0	0	19	3232	203	1044	43180	762	1352	0	0	0
CROMO2 115	10.92	0	14	0	0	0	2856	0	523	51917	961	1308	0	0	0
CROMO2 117	15.24	0	15	0	0	0	2479	188	270	49684	532	844	0	0	0
CROMO2 118	16.76	0	17	0	0	32	2682	296	498	48072	698	802	0	0	0
CROMO2 119	18.29	0	39	0	0	0	2218	187	1498	34664	1070	1217	0	0	0
CROMO2 120	19.81	59	480	0	0	39	640	0	10895	46082	1445	670	143	2406	409
CROMO2 121	21.34	51	447	9	0	42	1141	0	13084	60525	1444	1458	158	2058	2568
CROMO2 122	22.86	0	309	0	0	0	1708	0	8946	59767	1515	2227	98	810	416
CROMO2 123	24.38	28	479	11	0	48	2341	0	18169	58205	1160	2194	167	1920	2840
CROMO2 124	25.91	34	469	0	0	28	244	0	41369	52349	1371	198	153	3175	311
CROMO2 125	27.43	110	272	43	0	72	109	0	13547	56429	1288	292	242	3962	16065
CROMO2 126	28.96	78	388	27	0	97	864	0	24961	85300	1956	1404	230	3831	10454
CROMO2 127	30.48	68	562	18	0	42	626	0	14914	61254	1204	597	159	2990	5294
CROMO2 128	32.00	134	351	46	18	93	0	0	14152	61009	1364	62	251	4261	17266

Segment	Depth (m)	Zr	Sr	Rb	Pb	Zn	Ni	Co	Ca	Fe	Mn	Cr	V	Ti	K
CROMO2 129	33.53	113	339	45	9	59	0	0	13188	74521	1602	57	249	4478	17621
CROMO2 130	35.05	118	407	27	0	62	423	0	17954	50174	1197	370	163	3260	9445
CROMO2 131	36.58	64	674	11	9	44	535	175	14031	41952	1218	450	158	2313	3057
CROMO2 132	38.10	0	32	0	0	0	2469	0	964	53032	750	2941	0	169	294
CROMO2 133	39.62	0	15	0	0	0	2240	186	455	46986	511	768	0	0	0
CROMO2 134	41.15	0	14	0	0	0	1849	268	361	44132	442	827	0	0	0
CROMO2 135	42.67	0	11	0	0	0	2043	0	0	46199	605	1410	0	0	191
CROMO2 136	44.20	0	12	0	0	0	2403	213	443	48289	642	2450	0	129	0
CROMO2 137	45.72	0	6	0	0	0	1455	187	798	35024	570	494	0	67	0

Table 22

List of values of sequestered CO_2 masses for Mg as the only reactive cation, ordered by sequestration potential.

Values assigned to variables	kg CO_2 sequestered	MT CO_2 sequestered	tons CO_2 sequestered
20% olivine, 5 km depth, 2700 kg/m^3	4.60×10^{13}	4.60×10^{4}	5.07×10^{10}
30% olivine, 3.5 km depth, 2700 kg/m^3	4.83×10^{13}	4.83×10^{4}	5.33×10^{10}
30% olivine, 4 km depth, 2700 kg/m^3	5.52×10^{13}	5.52×10^{4}	6.09×10^{10}
25% olivine, 5 km depth, 2700 kg/m^3	5.75×10^{13}	5.75×10^{4}	6.34×10^{10}
30% olivine, 4.5 km depth, 2700 kg/m^3	6.22×10^{13}	6.22×10^{4}	6.85×10^{10}
30% olivine, 5 km depth, 2600 kg/m^3	6.65×10^{13}	6.65×10^{4}	7.33×10^{10}
30% olivine, 5 km depth, 2700 kg/m^3	6.91×10^{13}	6.91×10^{4}	7.61×10^{10}
30% olivine, 5 km depth, 2800 kg/m^3	7.16×10^{13}	7.16×10^{4}	7.89×10^{10}
30% olivine, 5 km depth, 2900 kg/m^3	7.42×10^{13}	7.42×10^{4}	8.18×10^{10}
30% olivine, 5.5 km depth, 2700 kg/m^3	7.60×10^{13}	7.60×10^{4}	8.37×10^{10}
30% olivine, 5 km depth, 3000 kg/m^3	7.67×10^{13}	7.67×10^{4}	8.46×10^{10}
35% olivine, 5 km depth, 2700 kg/m^3	8.06×10^{13}	8.06×10^{4}	8.88×10^{10}
40% olivine, 5 km depth, 2700 kg/m^3	9.21×10^{13}	9.21×10^{4}	1.01×10^{11}
Average	6.76×10^{13}	6.76×10^{4}	7.45×10^{10}

Table 23

List of values of sequestered CO_2 masses for Mg, Fe, and Ca, ordered by sequestration potential.

Values assigned to variables	kg CO_2 sequestered	MT CO_2 sequestered	tons CO_2 sequestered
20% olivine, 5 km depth, 2700 kg/m^3	6.18×10^{13}	6.18×10^{4}	6.81×10^{10}
30% olivine, 3.5 km depth, 2700 kg/m^3	6.49×10^{13}	6.49×10^{4}	7.15×10^{10}
30% olivine, 4 km depth, 2700 kg/m^3	7.41×10^{13}	7.41×10^{4}	8.17×10^{10}
25% olivine, 5 km depth, 2700 kg/m^3	7.72×10^{13}	7.72×10^{4}	8.51×10^{10}
30% olivine, 4.5 km depth, 2700 kg/m^3	8.34×10^{13}	8.34×10^{4}	9.19×10^{10}
30% olivine, 5 km depth, 2600 kg/m^3	8.92×10^{13}	8.92×10^{4}	9.84×10^{10}
30% olivine, 5 km depth, 2700 kg/m^3	9.27×10^{13}	9.27×10^{4}	1.02×10^{11}
30% olivine, 5 km depth, 2800 kg/m^3	9.61×10^{13}	9.61×10^{4}	1.06×10^{11}
30% olivine, 5 km depth, 2900 kg/m^3	9.95×10^{13}	9.95×10^{4}	1.10×10^{11}
30% olivine, 5.5 km depth, 2700 kg/m^3	1.02×10^{14}	1.02×10^{5}	1.12×10^{11}
30% olivine, 5 km depth, 3000 kg/m^3	1.03×10^{14}	1.03×10^{5}	1.14×10^{11}
35% olivine, 5 km depth, 2700 kg/m^3	1.08×10^{14}	1.08×10^{5}	1.19×10^{11}
40% olivine, 5 km depth, 2700 kg/m^3	1.24×10^{14}	1.24×10^{5}	1.36×10^{11}
Average	9.07×10^{13}	9.07×10^{4}	1.00×10^{11}

Table 24

Listing of maximum and minimum possible sequestered CO_2 values based on highest and lowest range of variables used.

Description	kg CO_2 sequestered	MT CO_2 sequestered	tons CO_2 sequestered
Mg only, shallowest depth, lowest olv %, least dense	4.16×10^{13}	4.16×10^{4}	4.59×10^{10}
Mg, Fe and Ca, greatest depth, highest olv %, most dense	1.51×10^{14}	1.51×10^{5}	1.66×10^{11}

Appendix B - Chemical Equations Used in this Paper

$2Mg_2SiO_4$ (forsteritic olivine) + CO_2 + $2H_2O$ → $Mg_3Si_2O_5(OH)_4$ + $MgCO_3$ (1)

Mg_2SiO_4 (forsteritic olivine) + $2CO_2$ + $2H_2O$ → $2MgCO_3$ + H_4SiO_4 (2)

$Mg_3Si_2O_5(OH)_4$ (serpentine)+ $3CO_2$ + $2H_2O$ → $3MgCO_3$ +$2H_4SiO_4$ (3)

Fe_2SiO_4 (fayalitic olivine) + $2CO_2$ + $2H_2O$ → $2FeCO_3$ + H_4SiO_4 (4)

$CaSiO_3$ (wollastonite) + CO_2 + $2H_2O$ → $CaCO_3$ + H_4SiO_4 (5)

CO_2 (g) + H_2O(l) → $H_2CO_3^-$(aq) (6)

$\frac{1}{3}Mg_3Si_2O_5(OH)_4 + 2H^+ \rightarrow Mg^{2+} + \frac{2}{3}SiO_2$ (aq) + $\frac{2}{3}H_2O$ (7)

$Mg_2SiO_{4\,(s)} + 4H^+ \rightarrow 2Mg^{2+} + H_4SiO_{4\,(aq)}$ (8)

$Mg^{2+} + HCO_3^- \rightarrow MgCO_3(s) + H^+$ (9)

RCO_2 (10)

$3Fe(OH)_2$ (iron(ii) hydroxide) → Fe_3O_4 (magnetite) + $2H_2O$(l) + H_2(g) (11)

$5Mg_2SiO_4$ (forsterite) + $9H_2O$(l) + Fe_2SiO_4 (fayalite) →

$3Mg_3Si_2O_5(OH)_4$ (serpentine) + $Mg(OH)_2$ (brucite) + $2Fe(OH)_2$

(iron(ii) hydroxide) (12)

$(Mg,Fe)_2SiO_4 + nH_2O + CO_2 \rightarrow Mg_3Si_2O_5(OH)_4 + Fe_3O_4 + CH_4$ (13)

$Mg_2SiO_4 + 4H^+ \rightarrow 2Mg^{2+} + H_4SiO_4$ (14)

$Mg^{2+} + HCO_3^- \rightarrow MgCO_3 + H^+$ (15)

$OH^- + H^+ \rightarrow H_2O$ (16)

Mg_2SiO_4 (forsteritic olivine) + $2HCO_3^- \rightarrow 2MgCO_3 + SiO_2 + 2OH^-$ (17)

$OH^- + CO_2 \rightarrow HCO_3^-$ (18)

Appendix C - *Ex Situ* vs. *In Situ* Carbon Sequestration Options

In situ and *ex situ* sequestration are both viable options for the Coast Range Ophiolite. There are certainly benefits and disadvantages to both, meriting exploration.

Ex situ sequestration is analogous to strip mining. During *ex situ* processing, rock must first be extracted from the underlying rock before it can be processed. The extraction itself is both a labor- and energy-intensive process, requiring removal of overlying soil and plant life. The amazing biodiversity of serpentine endemic plant and soil communities would make it difficult to justify this approach, particularly in conserved lands of any sort. Given the dearth of serpentine outcrops and soils in specific climates, removal of the endemic flora would prove highly controversial in addition to being environmentally deleterious.

A benefit of *ex situ* sequestration is that when an entire block of rock is extracted, it can be ground up to a diameter of a specific grain size, thereby increasing the surface area for chemical reactions—but this approach is not without costs. Decreasing the grain size of the rock requires copious amounts of grinding; the grinding process demands energy, which results in CO_2 generation, thus negating the entire motivation behind sequestration.

In the case of the Coast Range Ophiolite, the rocks of interest are at least 100 m below the surface. In related units elsewhere in the region, the olivine-rich peridotites may be even deeper beneath the surface. Removing shallow layers of olivine-poor serpentinite would require even more energy and destruction of landscape. Deeply buried olivine-rich lithologies, as at the McLaughlin locality of the

CRO, cause the cost of *ex situ* sequestration to escalate. Quarrying rocks may be more viable in cases of shallowly buried or exposed blocks of peridotites in deserts or other remote locations.

O'Connor et al. (2005) estimated to cost of sequestration for pure olivine at \$69/ton CO_2 sequestered. Serpentine carbonation costs were reduced to roughly \$78 per ton of CO_2 sequestered, including a necessary heat-treatment step prior to reacting the serpentine with CO_2. While thermal activation makes serpentine an effective medium of sequestration, the process results in more CO_2 generated than is sequestered by the process, making it impractical (O'Connor, 2005). The report does not mention if the cost and CO_2 generation figures include the process of mining the rocks. Mining is energy-intensive and surely would subtract from the benefits of the process.

Both *in situ* and *ex situ* sequestration generate carbonate minerals as a result of the chemical reaction, but *ex situ* processes allow access to the carbonate. Because *in situ* sequestration happens so far beneath the surface, access to the minerals is extremely limited. Industrial uses of magnesite, calcite and siderite include uses in antacids, construction materials, pigments, and cement-making.

In situ sequestration is seen as less environmentally deleterious, as it does not require the extraction of rock from the subsurface. Instead, holes of varying depth are drilled, and carbon-rich fluid is pumped deep into the subsurface where it is allowed to react freely with rocks. There are still untallied costs and energy inputs associated with *in situ* carbonation, yet there are simply fewer steps involved, thus

likely less cost in dollars. Part of those costs comes from the numerous holes that need to be drilled. Over a lengthy expanse of ultramafic rocks, thousands of holes would need to be drilled. Cost is also incurred through the necessary heating of rock prior to reaction. This is accomplished by pumping preheated water into a borehole. Costs can be considerably reduced if the exothermic reaction (Eq. 9) of carbonation preheats the surrounding rock and allows continuous heating throughout the process, eliminating the need for additional inputs of thermal energy.

Bibliography

Andreani M., Luquot L, Gouze P., Godard M., Hoisé M., Gibert B., 2008, Experimental Study of Carbon Sequestration Reactions Controlled by the Percolation of CO_2-Rich Brine Through Peridotites: Environ. Sci. Technol., 43, p. 1226-1231.

Beinlich A., Plumper O., Hovelmann, J., Austrheim H., Jamtveit B., 2012, Massive Serpentinite Cabonation at Linnajavri, N-Norway: Terra Nova, v. 00, no. 0, p. 1-10.

Boschi C., Dini A., Dallai L., Ruggieri G., Gianelli G., 2009, Enhanced CO_2-Mineral Sequestration by Cyclic Hydraulic Fracturing and Si-Rich Fluid Infiltration Into Serpentinites at Malentrata (Tuscany, Italy): Chemical Geology, 265, p. 209-226.

Caillaud J., Proust D., Righi D., 2006, Weathering Sequences of Rock-Forming Minerals in a Serpentinite: Influence of Microsystems on Clay Mineralogy: Clay and Clay Minerals, v. 54, no. 1, p. 87-100.

Choi, S.H., Shervais, J.W., Mukasa, S.B., 2008, Supra-Subduction and Abyssal Mantle Peridotites of the Coast Range Ophiolite, California: Contrib Mineral Petrol, v. 156, p.551-576.

Collins, M., An, S. I., Cai, W., Ganachaud, A., Guilyardi, E., Jin, F. F., Jochum M., Lengaigne M., Power S., Timmermann A., Vecchi G., Wittenberg, A., 2010, The Impact of Global Warming on the Tropical Pacific Ocean and El Niño. Nature Geoscience, vol. 3, p. 391-397.

Deer W.A., Howie R.A., Zussman J., 1966, An Intoduction to the Rock-Forming Minerals: Oxford, Longman Group.

Dessert, C., Dupre, B., Gaillardet, J., Francois, L. M. & Allegre, C. J., 2003, Basalt Weathering Laws and the Impact of Basalt Weathering on the Global Carbon Cycle: Chem. Geol., v. 202, p. 257–273.

Doney S.C., Ruckelshaus M., Duffy J.E., Barry J.P., Chan F., English C.A., Galindo H.M., Grebmeier J.M., Hollowed A.B., Knowlton N., Polovina J., Rabalais N.N., Syderman W.J., Talley L.D., 2012, Climate Change Impacts on Marine Ecosystems: Annual Review Marine Science, 4, p. 11–37.

Evans B.W., 2008, Control of the Products of Serpentinization by the $Fe^{2+}Mg_{-1}$ Exchange Potential of Olivine and Orthopyroxene: Journal of Petrology 49, p. 1873-1887.

Evans B.W., 2010, Lizardite versus Antigorite Serpentinite: Magnetite, Hydrogen, and Life(?): Geology, v. 38 p. 879-882.

Fetter Jr. C.W., 1980, Applied Hydrogeology: Columbus, C.E. Merrill.

Gerdemann S.J., O'Connor W.K., Dahlin D.C., Penner L.R. Rush H., 2007, Ex Situ Aqueous Mineral Carbonation: Environ. Sci. Technol, 41, p. 2587-2593.

Gislason, S., Wolff-Boenisch S., Stefansson A., Oelkers E., Gunnlaugsson E., Sigurdardottir H., Sigfusson B., Broecker W., Matter J., Stute M., Axelsson G., Fridriksson T., 2010, Mineral sequestration of Carbon Dioxide in Basalt: A Pre-Injection Overview of the CarbFix Project: International Journal of Greenhouse Gas Control. v. 4, iss. 3, p. 537-545.

Goff F., Guthrie G., Lipin B., Fite M., Chipera S., Counce D., Kluk E., Ziock H., 2000, Evaluation of Ultramafic Deposits in the Eastern United States and Puerto Rico as Sources of Magnesium for Carbon Dioxide Sequestration: Report *LA-13694-MS* for the Los Alamos National Laboratory, Department of Energy.

Goff F., Bergfeld D., Janik C.,Counce D., Stimac J.A., 2001, Geochemical Data on Waters, Gases, Rocks and Sediments From The Geysers–Clear Lake Region, California (1991-2000): Report *LA-13882-MS* for the Los Alamos National Laboratory, Department of Energy.

Goldberg D.S., Kent D.V., Olsen P.E., 2009, Potential On-Shore and Off-Shore Reservoirs for CO_2 Sequestration in Central Atlantic Magmatic Province Basalts:Proceedings of the National Academy of Sciences 107, no. 4, p. 1327-1332.

Goldberg P., Chen Z.Y., O'Connor W., Walters R., Ziock H., 2001, CO_2 Mineral Sequestration Studies in US: NETL Report for the Department of Energy.

González-Mancera G., Proenza Fernández J.A., Ortega-Gutiérrez F., 2007, Electron Microprobe Study of Zoned Chromite in Serpentinite from Tehuitzingo (Acatlán Complex, Southern Mexico). A Discussion over Its Origin: Acta Microscopia, vol. 16, no. 1-2 (Supp. 2), p. 296-297.

Green Mag Group. Media Release. http://scinews.com.au/releases/410/view (accessed 12/12/2011)

Herzog, H., 2009, "Carbon Dioxide Capture and Storage" in the Economics and Politics of Climate Change, Dieter Helm and Cameron Hepburn, eds, Oxford: Oxford University Press, p263-283.

IPCC Special Report, 2000, Emissions Scenarios Summary for Policymakers.

Jayko, A.S., Blake Jr. M.C., Harms T., 1987, Attenuation of the Coast Range Ophiolite by Extensional Faulting, and Nature of the Coast Range "Thrust", California: Tectonics, v. 6, no. 4, p. 475-488.

Kelemen P.B and Matter J.M., 2008, In Situ Carbonation of Peridotite for CO_2 Storage: PNAS, v. 105, no. 45, p. 17295-17300.

Krevor S.C.M., Lackner K.S., 2011, Enhancing Serpentine Dissolution Kinetics for Mineral Carbon Dioxide Sequestration: International Journal of Greenhouse Gas Control, no. 5, p. 1073-1080.

Mathez, E. A., 2009, Climate Change: The Science of Global Warming and Our Energy Future: New York, Columbia UP.

Matter J.M., and Kelemen P.B., 2009, Permanent Storage of Carbon Dioxide in Geological Reservoirs by Mineral Carbonation: Nature, v. 2, p. 837-841.

McLaughlin R.J., Blake Jr. M.C., Griscom A., Blome C.D., Murchey B., 1988, Tectonics of the Coast Range Ophiolite of California: Tectonics, v. 7, no.5, p. 1033-1056.

Moody, J., 1976, Serpentinization: A Review: Lithos, v. 9, iss. 2, p. 125-138.

NAS, Understanding and Responding to Climate Change, Highlights of the National Academies Reports: The National Academies- National Academy of Sciences, National Academy of Engineering, Institute of Medicine, National Research Council, 2008.

Nasir S., Al Sayigh A.R., Al Harthy A., Al-Khirbash S., Al-Jaaidi O., Musllam A., Al-Mishwat A., Al-Bu'saidi S., 2007. Mineralogical and Geochemical Characterization of Listwaenite From the Semail Ophiolite, Oman: Chemie der Erde – Geochemistry, v. 67, iss. 3, p. 213-228.

NOAA/ESRL (www.esrl.noaa.gov/gmd/ccgg/trends/)

O'Connor W.K., Dahlin D.C., Nilsen, G.E. Rush, R.P. Walters, Turner P.C., 2001, Carbon Dioxide Sequestration by Direct Mineral Carbonation: Results from Recent Studies and Current Status: United States Department of Energy, Office of Fossil Energy, Albany Research Center.

Oze C., Sharma N., 2005, Have Olivine, Will Gas: Serpentinization and the Abiogenic Production of Methane on Mars: Geophysical Research Letters, v. 32, li. 0203, p. 1-4.

Park A., Fan L., 2004, CO_2 Mineral Sequestration: Physically Activated Dissolution of Serpentine and pH Swing Process: Chemical Engineering Science, v. 59, iss. 22-23, p. 5241-5247.

Peters, E.K., 1993, D-^{18}O enriched waters of the Coast Range Mountains, northern California: Connate and ore-forming fluids. *Geochimica et Cosmochimica Acta* v. 57, iss 5, p. 1093-1104.

Richardson K., Steffen W., Schellnhuber H.J., Alcamo J., Barker T., Kammen D.M., Leemans R., Liverman D., Munasinghe M., Osman-Elasha B., Stern N., Wæver O., 2009, Synthesis Report: From the Climate Change: Global Risks, Challenges, and Decisions Conference, Copenhagen, International Alliance of Research Universities.

Ruddiman W. F., 2001, Earth's Climate: Past and Future: New York, W.H. Freeman & Sons.

Shervais J.W., Kimbrough, D.L., 1985, Geochemical Evidence for the Tectonic Setting of the Coast Range Ophiolite: A composite Island Arc –Oceanic Crust Terrane in Western California: Geology, v. 13, no. 1, p. 35-38.

Shervais J.W., Kimbrough D.L., Renne P., Hanan B.B., Murchey B., Snow C.A., Schuman M.M.Z., and Beaman J., 2004, Multi-Stage Origin of the Coast Range Ophiolite, California: Implications for the Life Cycle of Supra-Subduction Zone Ophiolites: International Geology Review, v. 46, p. 289-315.

Schulte M., Blake D., Hoehler T.M., McCollom T., 2006: Serpentinization and Its Implications for Life on the Early Earth and Mars :Astrobiology, Apr; 6(2), p.364-76.

Shervais J.W., Kimbrough, D.L., 1985, Geochemical Evidence for the Tectonic Setting of the Coast Range Ophiolite: A composite Island Arc –Oceanic Crust Terrane in Western California: Geology, v. 13, no. 1, p. 35-38.

Smith J.B., Schneider S.H., Oppenheimer M., Yohe G.W., Hare W., Mastrandrea M.D., Patwardhan A., Burton I., Corfee-Morlot J., Magadza C.H.D., Fussel H.-M., Pittock A.B., Rahman A., Suarez A., van Ypersele J.-P., 2009, Assessing Dangerous Climate Change Through an Update of the Intergovernmental Panel on Climate Change (IPCC) ‘‘Reasons for Concern”: PNAS, Early Edition, p. 1-5.

Solomon, S., Qin D., Manning M., Chen Z., Marquis M., Avery K.B., Tignor M., Miller H.L., 2007, Contribution of Working Group I to the Fourth Assessment Report of the Intergovernmental Panel on Climate Change: IPCC.

Strand S., Benford G., 2009, Ocean Sequestration of Crop Residue Carbon: Recycling Fossil Fuel Carbon Back to Deep Sediments: Environ. Sci. Technol, v. 43, no.4, p. 1000–1007.

Strong A. L., Cullen J.J., Chisholm S.W., 2009, Ocean Fertilization Science, Policy, and Commerce: Oceanography, vol. 22, no. 3, p. 236-261.

Thornton, P., 2012, Recalibrating Food Production in the Developing World: Global Warming Will Change More Than Just the Climate, CCAFS Policy Brief, no. 6, CGIAR Research Program on Climate Change, Agriculture and Food Security (CCAFS), p. 1-16.

Ulmer G. C., 1974, Alteration of Chromite During Serpentinization in the Pennsylvania-Maryland District: American Mineralogist, vol. 59, p. 1236-1241.

USGS, 1987, Mineral Resources Online Spatial Data: Franciscan Complex, Unit 1 (Coast Ranges): http://tin.er.usgs.gov/geology/state/sgmc-unit.php?unit=CAKJf1%3B0

Wakabayashi J., Dilek Y., 2000, Spatial and Temporal Relationships Between Ophiolites and Their Metamorphic Soles: A Test of Models of Forearc Ophiolite Genesis: Geological Society of America Special Paper 349, p. 53-64.

Wicks F.J., Whittaker E.J., 1977, Serpentine Textures and Serpentinization: Canadian Mineralogist, vol. 15, p. 459-488.

Xu, T., Apps, J. A., Pruess, K., 2004, Numerical Simulation of CO_2 Disposal by Mineral Trapping in Deep Aquifers: Appl. Geochem. v. 19, p. 917–936.